Cone bipolar cell synapses generate transient versus sustained signals in parallel ON pathways of the mouse retina

Sidney P. Kuo[1,2], Wan-Qing Yu[1], Prerna Srivastava[3], Haruhisa Okawa[1], Luca Della Santina[1], David M. Berson[4], Gautam B. Awatramani[3], Rachel O.L. Wong[1], Fred Rieke[1]

[1]Department of Neurobiology and Biophysics, University of Washington, Seattle WA
[2]Department of Neuroscience, University of Minnesota, Minneapolis MN
[3]Department of Biology, University of Victoria, Victoria BC
[4]Department of Neuroscience, Brown University, Providence RI

Correspondence: Fred Rieke, rieke@uw.edu

Abstract

Parallel processing is a fundamental organizing principle in the nervous system and understanding how parallel neural circuits generate distinct outputs from common inputs is a key goal of neuroscience. In the mammalian retina, divergence of cone signals into multiple feedforward bipolar cell pathways forms the initial basis for parallel retinal circuits dedicated to specific visual functions. Here, we used patch-clamp electrophysiology, electron microscopy and two photon imaging of a fluorescent glutamate sensor to examine how kinetically-distinct responses arise in transient versus sustained ON alpha RGCs (ON-T and ON-S RGCs) of the mouse retina. We directly compared the visual response properties of these RGCs with their presynaptic bipolar cell partners, which we identified using 3D electron microscopy reconstruction. Different ON bipolar cell subtypes (type 5i, type 6 and type 7) had indistinguishable light-driven responses whereas extracellular glutamate signals around RGC dendrites and postsynaptic excitatory currents measured in ON-T and ON-S RGCs in response to the identical stimuli used to probe bipolar cells were kinetically distinct. Anatomical examination of the bipolar cell axon terminals presynaptic to ON-T and ON-S RGCs suggests that bipolar subtype-specific differences in the size of synaptic ribbon-associated vesicle pools may contribute to transient versus sustained kinetics. Our findings indicate that feedforward bipolar cell synapses are a primary point of divergence in kinetically distinct visual pathways.

Introduction

Divergence into parallel pathways allows neural circuits to generate diverse outputs from a common set of inputs. This functional diversity can be quite striking; in vision, for example, light inputs initially encoded by the same collection of cone photoreceptors mediate sensitivity to several kinds of motion, to color and to spatial structure, all in the same region of space. These diverse functional sensitivities arise through parallel processing of light inputs, first in the retina and subsequently in downstream visual areas. Here we focus on the origin of transient and sustained responses – a key differentiating characteristic of retinal output cells across species (Awatramani and Slaughter, 2000; Baden et al., 2016; Bae et al., 2018; Cleland et al., 1973; Ikeda and Wright, 1972; Roska and Werblin, 2001; Werblin, 1970).

The retina provides a unique opportunity to study the mechanisms that differentiate signals in parallel pathways. We have a near-complete list of retinal cell types and substantial information about which of these cell types participate in specific parallel pathways (Helmstaedter et al., 2013; Masland, 2012). Under daylight conditions, retinal processing starts with cone photoreceptors transducing light inputs and providing divergent output to ~13 types of bipolar cell (Euler et al., 2014; Greene et al., 2016; Helmstaedter et al., 2013; Shekhar et al., 2016; Tsukamoto and Omi, 2017). The resulting bipolar cell signals are transmitted to ~20-40 retinal ganglion cell (RGC) types (Baden et al., 2016; Bae et al., 2018; Goetz et al., 2022). RGC responses are also strongly shaped by the activity of a large and diverse collection of amacrine cells that receive input from bipolar cells and provide presynaptic inhibition to bipolar cells and postsynaptic inhibition to RGCs (Diamond, 2017; Jadzinsky and Baccus, 2013). Finally, RGC responses are shaped by feedforward synaptic properties, particularly synaptic depression and facilitation (DeVries, 2000; Grabner et al., 2016; Jarsky et al., 2011; Lagnado and Schmitz, 2015; Nikolaev et al., 2013; Oesch and Diamond, 2011).

These mechanisms collectively produce highly distinct responses across RGC types - with cells that sample inputs on a variety of spatial and temporal scales, cells with distinct chromatic properties, cells that sense the direction of moving objects, and cells that separate local from

global motion (reviewed by Gollisch and Meister, 2010; Kerschensteiner, 2022). Several mechanisms contribute to these functional differences, starting with the division of signals into ON and OFF pathways at the cone-to-bipolar synapse (Euler et al., 2014; Slaughter and Miller, 1981). Temporal properties of responses of different bipolar cells can also differ for some stimuli (Awatramani and Slaughter, 2000; Baden et al., 2013; Euler et al., 2014; Euler and Masland, 2000; Ichinose et al., 2014; Ichinose and Hellmer, 2016; Wu et al., 2000). In the inner retina, integration of excitatory and inhibitory synaptic inputs produces directionally-selective responses in specific RGC types (Taylor and Vaney, 2002; Vaney et al., 2012) and differences in spatial weighting functions in other RGCs (Cafaro and Rieke, 2013; Roska and Werblin, 2001; Zhang et al., 2012). Properties of dendritic integration and RGC spike generation also differentiate responses of some RGCs (Margolis et al., 2010; Ran et al., 2020; Wienbar and Schwartz, 2022).

A fundamental difference among RGCs is whether their responses are sustained or transient (Awatramani and Slaughter, 2000; Baden et al., 2016; Bae et al., 2018; Cleland et al., 1973; Ikeda and Wright, 1972; Roska and Werblin, 2001). Cone photoreceptors respond to changes in light intensity with graded potentials that have both a transient and sustained component (Angueyra and Rieke, 2013; Cangiano et al., 2012; Szikra et al., 2014). Both kinetic components of the cone response are maintained in the firing rates of sustained cells, which track the prevailing contrast. However, only the initial component of the cone response is preserved in the spiking response of transient cells, which therefore respond primarily to changes in contrast. Where and how these differences originate is not clear. Here, we show that the distinct kinetics of responses of ON-sustained alpha and ON-transient alpha RGCs (1) persist for stimuli that elicit near-identical responses among the relevant bipolar cells, (2) persist without amacrine cell-mediated inhibition and, (3) are correlated with anatomical differences in output synapses of bipolar cell subtypes that are presynaptic to these RGCs. These findings highlight the importance of feedforward bipolar cell output synapses in producing kinetically distinct retinal outputs.

Results

We focused on two ON RGC cell types, ON-transient alpha (ON-T) and ON-sustained alpha (ON-S) RGCs, that could be readily identified in a flat-mount preparation of the isolated mouse retina (Fig. 1A) by their characteristic spiking response to a step increment in light intensity (Fig. 1B) (Bae et al., 2018; Farrow et al., 2013; Goetz et al., 2022; Krieger et al., 2017; Kuo et al., 2016). Based on their light response, dendritic field size and stratification pattern in the inner plexiform layer (IPL) (see below; Fig. S4), the ON-T RGCs we studied here likely correspond to the PV2 RGC type of Farrow et al. (2013), 6sw RGC type of Bae et al. (2018) and the medium-field ON-transient RGC of Goetz et al. (2022). ON-S RGCs correspond to the PV1 RGC type of Farrow et al. (2013) and 8w RGC type of Bae et al. (2018).

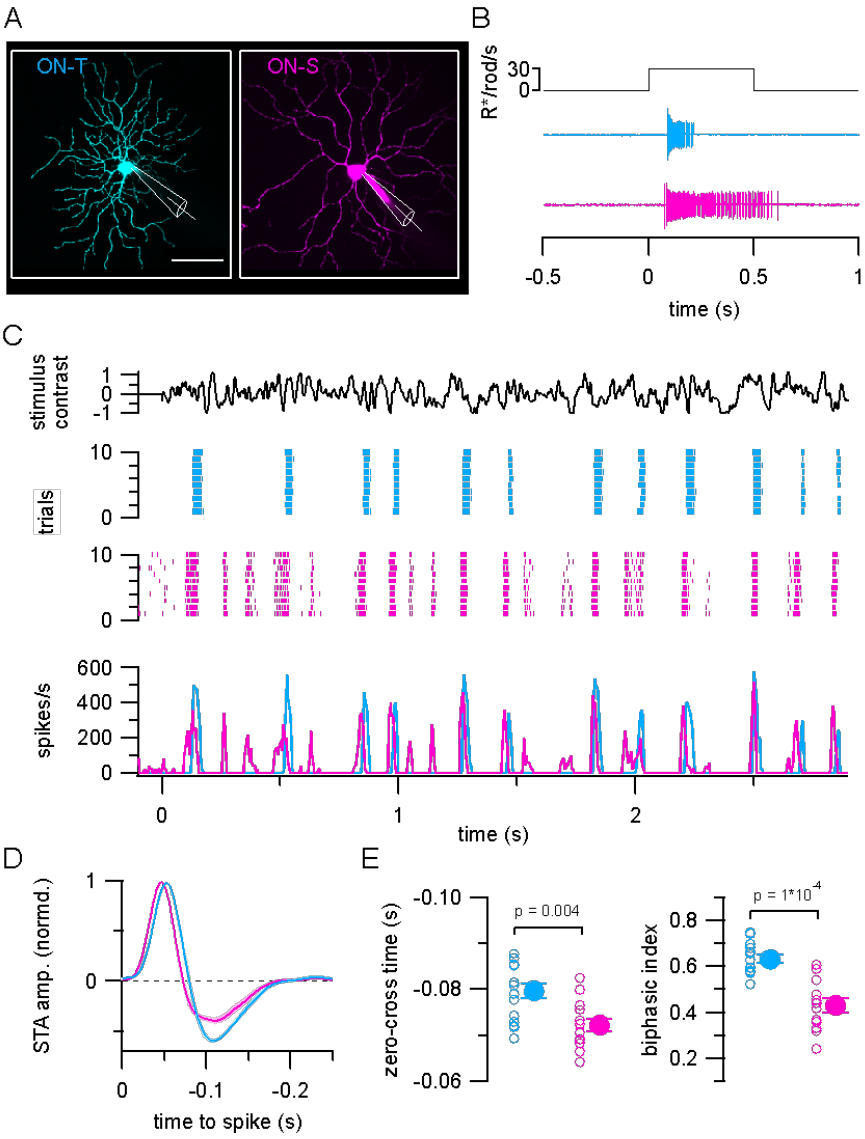

***Figure 1**. Distinct temporal spiking response properties of ON-transient (ON-T) versus ON-sustained (ON-S) RGCs. (A) Maximum intensity projection z-stack fluorescence images of ON-T (left, cyan) and ON-S (right, magenta) RGCs dialyzed with Alexa Fluor 594 during whole-cell patch-clamp recording. Scale bar 50 µm. (B) Characteristic spiking responses to a light increment for example ON-T and ON-S RGCs. (C) Example spiking responses to repeated trials of spatially uniform (52 0 µm spot diameter) Gaussian noise stimulus (top black trace) presented with a mean luminance of ~20 00 P*/S-cone/s (~33 00 R*/rod/s; ~1650 P*/M-cone/s). ON-T (cyan) and ON-S (magenta) RGCs were recorded sequentially in the same piece of retina. Average spike responses (bottom) calculated from 20 repetitions of the noise stimulus. (D) ON-T and ON-S STAs derived from responses to non-repeated noise stimuli. Colored lines and shaded areas show mean ± SEM STA waveforms from ON-T (n= 15) and ON-S (n= 13) RGCs. The STA time axis is reversed to facilitate comparison with linear filters in Figures 2 and 4. The mean line obscures the SEM shading for much of the filter in both cell types. (E) Quantification of STA kinetics in different RGCs. Open circles show measurements from individual cells and filled circles with error bars show mean ± SEM values. Significance values from Wilcoxon rank sum tests.*

We characterized the temporal spiking response properties of ON-T and ON-S RGCs by using an extracellular cell-attached patch electrode to measure action potential firing from either cell type while presenting a spatially uniform, randomly fluctuating light stimulus (Gaussian noise) that allowed us to efficiently probe a variety of stimulus contrasts and temporal frequencies. These and all subsequent physiological recordings were conducted using a photopic mean background light level (~3300 R*/rod/s; ~2000 P*/S-cone/s; ~1650 P*/M-cone/s) to suppress rod photoreceptor responses and focus on cone-mediated signaling (Grimes et al., 2018; Ke et al., 2014). Figure 1C shows the spiking response of example ON-T and ON-S RGCs to multiple repetitions of the same random stimulus contrast sequence; these RGC types clearly responded differently to temporally modulated light input. In particular, noise-evoked ON-T RGC spike responses were comprised primarily of large amplitude, less frequent spike bursts whereas ON-S RGC responses were less discrete and consisted of events with a wider range of amplitudes (Fig. 1C and Fig S1A).

We summarized the response of each ON-T and ON-S RGC by computing the average stimulus preceding each recorded spike (the spike-triggered average or STA stimulus) when presenting a non-repeated Gaussian noise stimulus (Fig. 1D) (Chichilnisky, 2001). W e quantified response kinetics from these STA waveforms by measuring the time of zero-crossing (between trough and peak) as well as the ratio of amplitudes of the trough and peak (biphasic index). ON-T RGC STAs were significantly more biphasic (biphasic index = 0.63 ± 0.07; mean ± S.D.; n = 15) than ON-S RGC STAs (biphasic index = 0.43 ± 0.11; mean ± S.D.; n = 13) (Fig. 1E, right), consistent with their more transient responses to step stimuli (Fig. 1B). ON-T RGC responses were also slightly delayed (zero-cross time = - 0.080 ± 0.0063 sec; mean ± S.D.; n = 15) relative to those of ON-S RGCs (zero-cross time = -0.072 ± 0.0052 sec; mean ± S.D.; n = 13) (Fig. 1C, bottom and 1E, left). The STA provides a convenient summary of RGC temporal response properties, but it does not capture all differences between the RGC spike responses – e.g. the discreteness of the ON-T responses in Figure 1C. Nonetheless, the combination of direct observation of the spike responses and STA kinetics illustrate how ON-S and ON-T responses differ.

Bipolar cell to RGC synapses are an important site of signal diversification in ON pathways

A variety of mechanisms could contribute to the distinct temporal response characteristics of ON-T versus ON-S RGCs, including differences in excitatory and/or inhibitory input conveyed by presynaptic circuits. Parallel visual channels are initially established by the divergence of cone signals to different cone bipolar cell subtypes, which have axons that terminate at distinct depths within the IPL and can correspondingly contact distinct RGC types (Euler et al., 2014; Wässle et al., 2009). Prior studies have demonstrated IPL layer-specific light-evoked glutamate release kinetics from different bipolar cell synaptic terminals (Borghuis et al., 2013a; Franke et al., 2017). We therefore sought to understand to what extent kinetic differences in bipolar cell-mediated excitatory synaptic input could account for the transient versus sustained responses of these RGCs.

To do this, we used somatic whole-cell voltage-clamp recordings to measure excitatory synaptic currents from both RGC types while stimulating the retina with the same spatially uniform Gaussian noise stimulus that we used to characterize RGC spike output (Fig. 2A). We used these measurements to construct linear-nonlinear (LN) models comprised of a linear temporal filter (Fig. 2B and Fig. S2A) and a time-invariant (static) nonlinearity (Fig. S2B) that together provide a simple estimate of the transformation between visual input and excitatory synaptic input to each RGC type (Kim and Rieke, 2001). LN models for each RGC type accurately predicted measured

responses to noise stimuli that were not used to construct the models, although LN models of ON-S RGC responses performed better than those for ON-T RGCs (correlation coefficient between average response to repeated noise stimulus and model prediction: 0.61 ± 0.06 (ON-S, n = 9) and 0.50 ± 0.13 (ON-T, n =11), mean ± S.D.; p = 0.028 Wilcoxon rank-sum test). ON-T stimulus-evoked excitatory currents were biased towards large amplitude events compared to those of ON-S RGCs (Fig. 2A, Fig. S1B), like the distinct amplitude distributions of spike events in these cell types noted above (Fig. 1C and Fig. S1A).

The linear filter captures the kinetics of the RGC response and is analogous to the time-reversed STA derived from spike responses (Chichilnisky, 2001). As with the STAs in Figure 1D, excitatory linear filters were slower and more biphasic in ON-T (zero-cross time = 0.10 ± 0.013 s; biphasic ind. = 0.45 ± 0.090; mean ± S.D.; n = 13) compared to ON-S RGCs (zero-cross time = 0.083 ± 0.0074 s; biphasic ind. = 0.31 ± 0.10; mean ± S.D.; n = 15) (Fig. 2C). This latter difference is consistent with more transient light-evoked excitatory synaptic input to ON-T RGCs. Indeed, light step-evoked excitatory currents to ON-T RGCs decayed to baseline levels within a few hundred milliseconds, even in the continued presence of light input, whereas excitatory inputs to ON-S RGCs had a sustained component that persisted for the duration of the light step (Fig. 2D-E).

These results show that transient versus sustained kinetics are already present in the excitatory pathways that provide input to ON-T and ON-S RGCs. However, these findings do not rule out additional contributions to the distinct spiking behavior of these RGC types from amacrine cell-mediated inhibitory synaptic input to the RGCs or from different intrinsic spiking properties. To examine whether postsynaptic inhibition contributes importantly to kinetic differences between ON-T and ON-S RGCs, we measured both excitatory and inhibitory synaptic currents in response to Gaussian noise stimuli in a subset of RGC recordings (Fig. S3). Like excitatory currents, light-evoked inhibitory currents were more transient in ON-T RGCs (linear filter biphasic ind. = 0.34 ± 0.12; mean ± S.D.; n= 8) compared to those in ON-S RGCs (biphasic ind. = 0.16 ± 0.09; mean ± S.D.; n= 8) (Fig. S3B-C; p= 0.01, Wilcoxon rank sum test). We also quantified the relative strength of excitatory and inhibitory synaptic inputs by calculating the ratio between the largest noise-evoked excitatory and inhibitory conductances (G_{exc} and G_{inh}; derived from the measured currents) in response to a repeated noise stimulus in each RGC (Fig. S3A, D-E). This ratio did not differ significantly between the two cell types (ON-T RGCs: peak G_{exc} / peak G_{inh} = 1.46 ± 0.65; mean ± S.D.; n = 6; ON-S RGCs: peak G_{exc} / peak G_{inh} = 4.04 ± 2.48; mean ± S.D.; n = 7; p=0.10, Wilcoxon rank sum test). The relatively small inhibitory inputs together with the clear differences we observed in excitatory synaptic input between ON-T and ON-S RGCs indicate that bipolar cell pathways have a central role in establishing transient versus sustained kinetics.

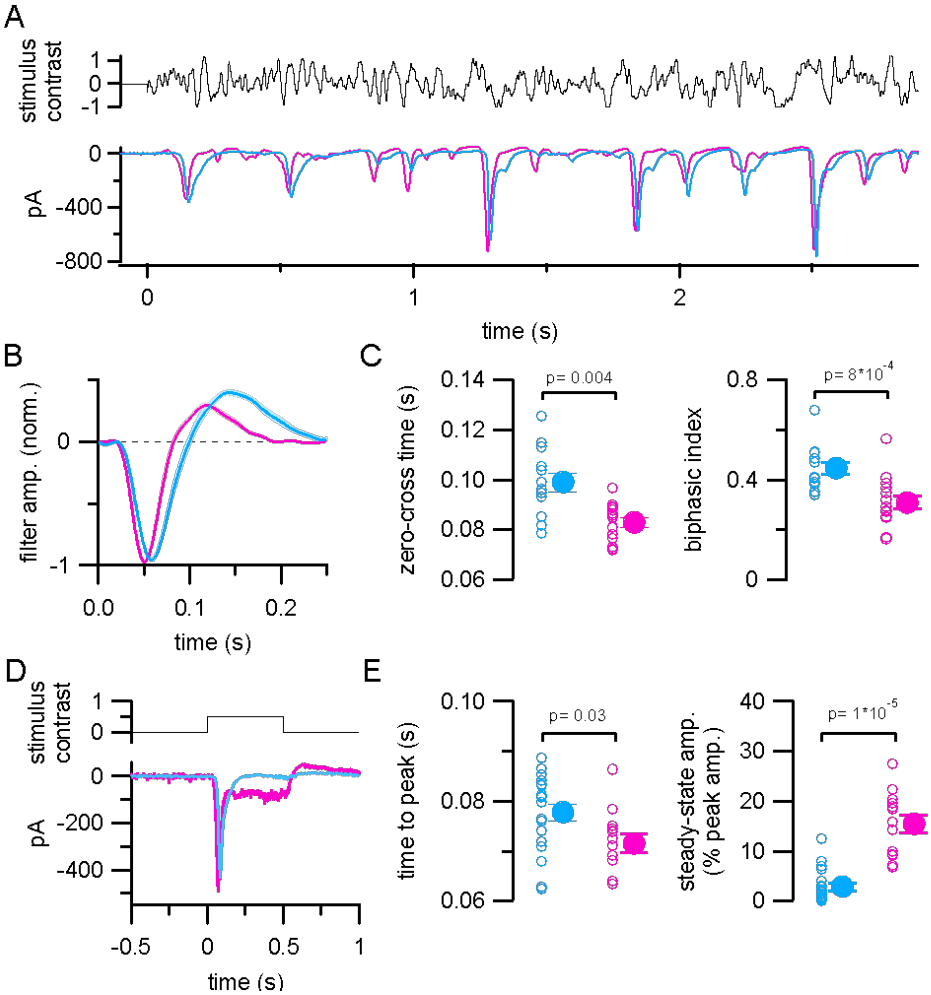

***Figure 2**. Distinct excitatory synaptic input to ON-T and ON-S RGCs. (A) Excitatory synaptic currents measured in example ON-T (cyan) and ON-S (pink) RGCs in response to the same Gaussian noise stimulus used in Fig. 1. Traces show average currents from ten repetitions of the same stimulus and are baseline subtracted to facilitate comparison. (B) Linear filters computed from responses to non-repeated noise stimulus presentation. Lines and shaded areas show mean ± SEM of responses from ON-T (n= 13) and ON-S (n= 15) RGCs. The mean line obscures the SEM shading for much of the filter in both cell types. (C) Quantification of filter kinetics in different RGCs. (D) Excitatory currents measured from example ON-T and ON-S RGCs in response to a 0.5 second step increase in light intensity (50% contrast; mean response to five repetitions of stimulus). (E) Quantification of step response kinetics (n= 19 ON-T RGCs; n= 13 ON-S RGCs). In (C) and (E) open circles show measurements from individual cells and filled circles with error bars show mean ± SEM values. Significance values from Wilcoxon rank sum tests.*

ON-T and ON-S RGCs receive input from distinct bipolar types

Retinal circuits dedicated to transient versus sustained signaling are generally located at the center and borders of the IPL (Baden et al., 2016; Bae et al., 2018; Beaudoin et al., 2019; Borghuis et al., 2013b; Franke et al., 2017; Roska and Werblin, 2001). We compared stratification patterns of ON-T and ON-S RGCs in a subset of whole-cell recordings by filling cells with a fluorescent

236 dye and imaging the dendrites of physiologically-characterized RGCs using two-photon
237 microscopy. We assessed IPL depth in live tissue by using retinas from a transgenic mouse line
238 in which type 5 bipolar cells strongly express EGFP (*Gjd2-EGFP* mice). These EGFP+ bipolar
239 cells express calcium binding protein 5 (CaBP5; Fig. S3B-D) and have axons that occupy a narrow
240 band just above and overlapping with the dendrites of ON starburst amacrine cells (Fig. S3A)
241 (Ghosh et al., 2004). Based on the regular spacing of their somas, these cells likely correspond
242 to one of the three subtypes of type 5 bipolar cells previously identified in mouse retina (Greene
243 et al., 2016; Rodieck, 1991) (Fig. S3E-F). Imaging of RGCs together with EGFP+ axon terminals
244 in *Gjd2-EGFP* mice revealed that ON-T and ON-S RGC dendrites occupy distinct, mostly non-
245 overlapping regions of the IPL (Fig. S4).
246
247 The distinct IPL stratification of ON-T and ON-S RGCs indicates they receive input from different
248 bipolar cell populations. Recent serial block-face electron microscopy (SBFSEM) connectomic
249 analyses found that type 6 and type 7 bipolar cells account for ~50-52% and 46% of the excitatory
250 synapses formed upon ON-S RGC dendrites (Sabbah et al., 2018; Swygart et al., 2024).
251 However, the bipolar cell subtype(s) presynaptic to ON-T RGCs have not previously been
252 identified. Our observation that ON-T RGC dendrites occupy a narrow band in the IPL that
253 closely matches the stratification pattern of EGFP+ type 5 bipolar cell axons in *Gjd2-EGFP* mice
254 (Fig. S5) suggests that these bipolar cells likely provide a substantial fraction of the excitatory
255 input to ON-T RGCs. To test this possibility, we transfected retinas from *Gjd2-EGFP* mice with a
256 plasmid encoding PSD-95 fused to the red fluorescent reporter mCherry to label postsynaptic
257 sites of excitatory input (Fig. S5). We used confocal microscopy to quantify the fraction of
258 putative synapses, defined as sites with overlapping PSD-95 and EGFP fluorescent signals, that
259 arose from *Gjd2-EGFP*+ axon terminals (Schwartz et al., 2012). From this analysis, we concluded
260 that the labeled type 5 bipolar cells in *Gjd2-EGFP* mice provide ~40% of the ribbon synaptic input
261 to ON-T RGCs (Fig. S5D).
262
263 We next performed correlative fluorescence imaging and SBFSEM to identify which type 5 bipolar
264 subtype is labeled in Gjd2-EGFP mice and to further characterize what other bipolar cell types
265 provide the remaining input to ON-T RGCs. We first used 2P microscopy to image the dendritic
266 morphology of two dye-filled ON-T RGCs that were identified from their light-evoked spike
267 responses in flat-mounted retina from *Gjd2-EGFP* transgenic mice (Fig. 3A). After 2P imaging,
268 we fixed the retina and used the near infrared branding (NIRB) technique to create fiducial marks
269 in the tissue around the dye-filled ON-T RGCs (Bishop et al., 2011). After acquiring the SBFSEM
270 volume, we located the somas of the two ON-T RGCs using these fiducial marks and
271 reconstructed the dendritic arbors of both cells (e.g. Fig. 3B). The dendritic morphologies from
272 our EM reconstruction matched those from the light microscopy images. This suggests that we
273 successfully identified the two ON-T RGCs recorded physiologically in our EM volume. We chose
274 the two longest dendritic arbors from the RGC soma to the dendritic tip and identified all the
275 synapses from bipolar cells along these dendrites (Fig. 3C). We then reconstructed all the
276 presynaptic bipolar cells and classified them according to their axon morphology and stratification
277 (Fig. 3D). Careful examination of axonal tiling among type 5i, 5o and 5t subtypes provided
278 additional confirmation of the classification of these type 5 bipolar cells (Fig. S7A) (Greene et al.,
279 2016). When comparing the EM images with light microscopy images, it is clear that *GJD2-GFP*+
280 bipolar cells are type 5i bipolar cells (Fig. S7B).
281

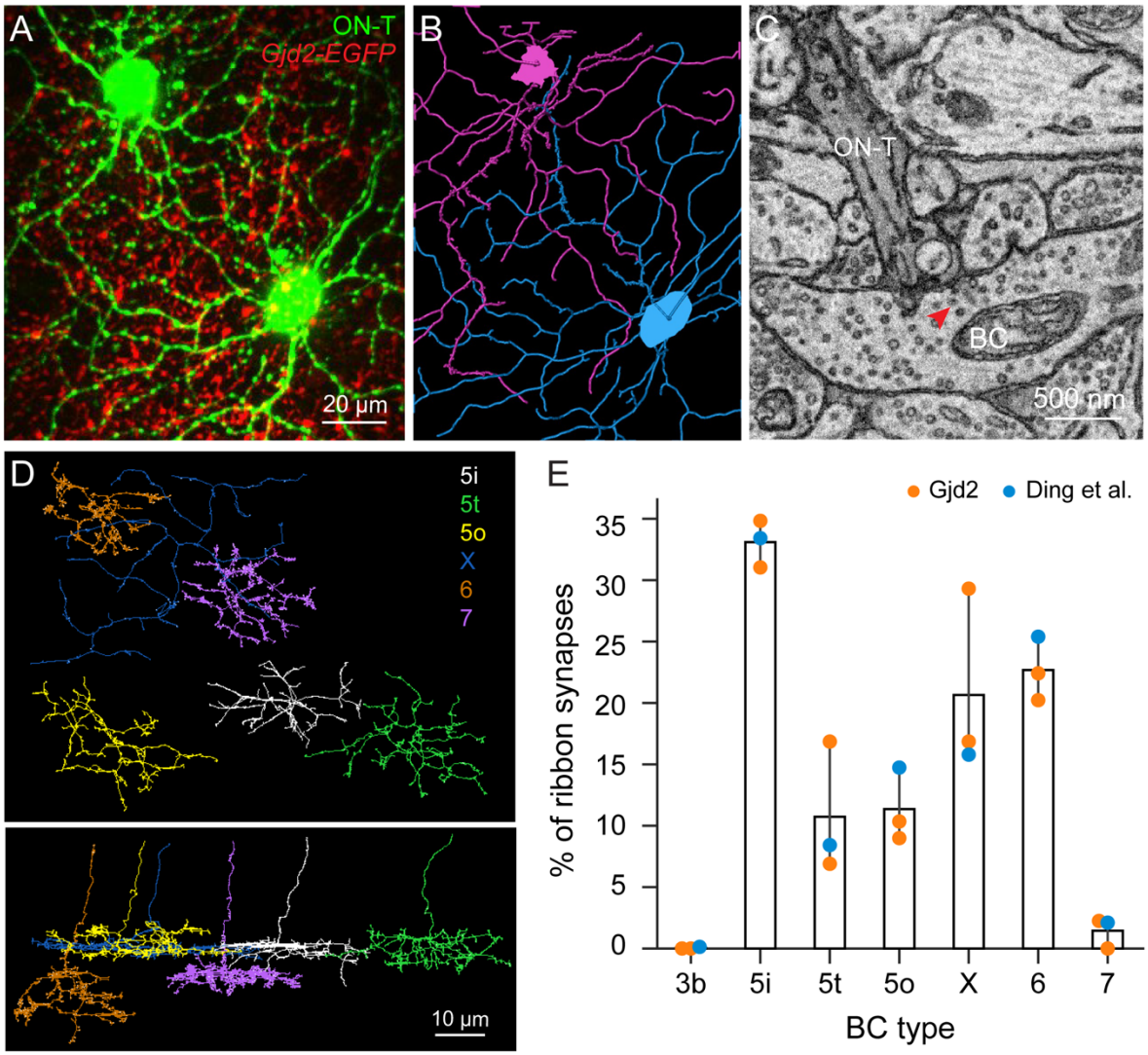

***Figure 3**. Identification of bipolar cell subtypes presynaptic to ON-T RGCs. (A) Maximum-projection z-stacks of two dye-filled ON-T RGCs (green) in wholemount retina from Gjd2-EGFP (red) transgenic mice. (B) Traced skeletons of dendritic arbors of the two ON-T RGCs from EM volume. (C) An EM micrograph showing a ribbon synapse (arrowhead) on a BC axonal terminal onto the dendrite of a ON-T RGC. (D) An example skeleton for each presynaptic BC type (types 5i, 5t, 5o, X, 6 and 7) of ON-T RGCs. Top: whole-mount view, Bottom: side view. (E) Bar plot showing the proportion of input synapses to ON-T RGCs from each BC type. Mean ± SEM (n=3 RGCs, 2 from this study and one from Ding et al. (2016)).*

Results from the SBFSEM reconstructions agreed closely with those from the light microscopy approach described above. Type 5i bipolar cell axon terminals provided the largest fraction of synapses onto the two ON-T RGCs within our SBFSEM volume (~30-35%). Other inputs arose from type 5o (~10%), type 5t (~5-15%), XBC (~15-30%), and, somewhat surprisingly given the differences in stratification, from type 6 (~20%) bipolar cells (Fig. 3E). We confirmed this connectivity pattern by additionally analyzing bipolar cell synaptic inputs to a putative ON-T RGC (RGC7089) in the same publicly available SBFSEM volume (Ding et al., 2016) that was used by Sabbah et al., (2018) to map inputs to ON-S RGCs (Fig. 3E).

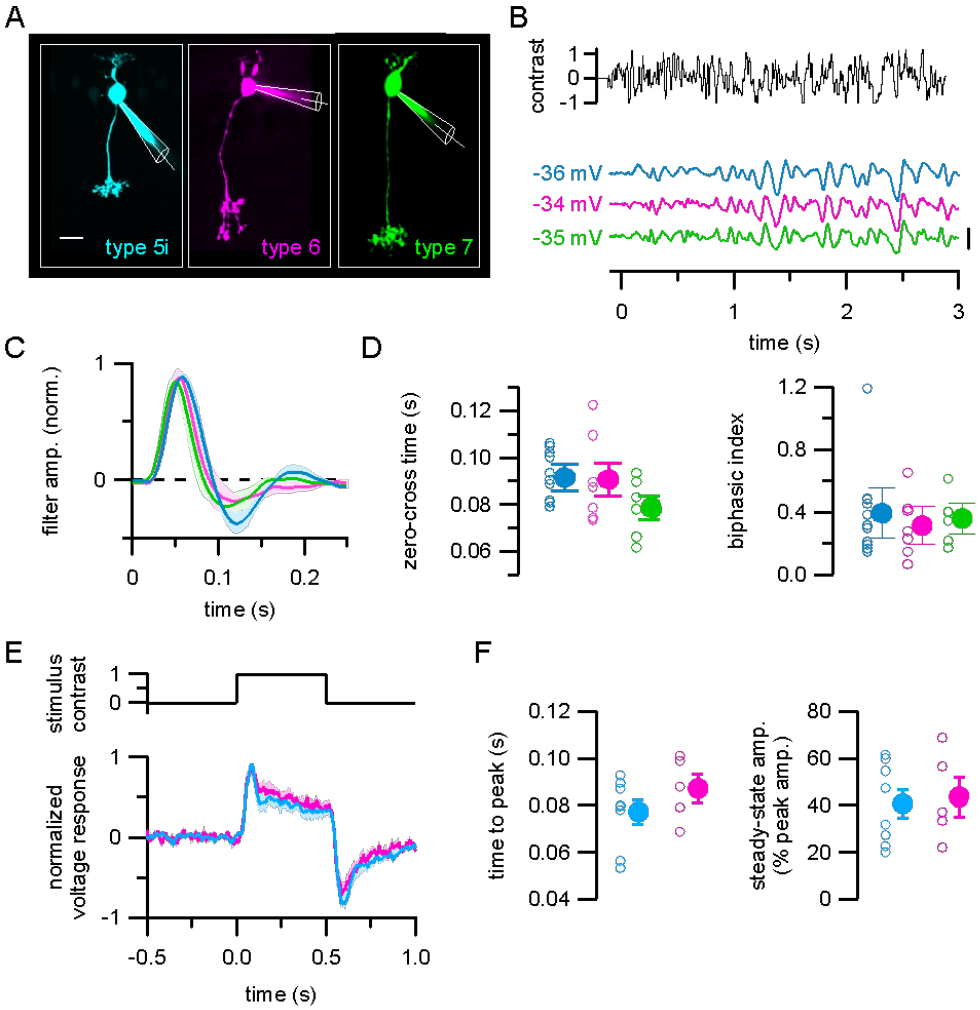

***Figure 4**. Bipolar cell subtypes presynaptic to ON-T and ON-S RGCs have indistinguishable temporal response properties. (A) Maximum-projection z-stacks of fluorescent dye-filled bipolar cells targeted for electrophysiological recording in retinal slices from Gjd2-EGFP (left), Grm6-tdTomato (middle), and Gus8.4-EGFP (right) transgenic mice. (B) Responses to spatially uniform Gaussian noise stimulation (same as in Figs. 1-2) in example type 5i (cyan), type 6 (magenta) and type 7 (green) bipolar cells. Voltage traces are average responses to ten repetitions of the noise stimulus. Scale bar = 5 mV. (C) Linear filters computed from responses to non-repeated noise stimulus presentation. Lines and shaded areas show mean ± SEM of responses (type 5i, n= 11; type 6, n= 7; type 7, n= 6). (D) Quantification of response kinetics from linear filters. No significant differences across types (p = 0.19 zero-cross times; p= 0.89 biphasic index; Kruskal-Wallis test). (E) Responses to step light increment. Lines and shaded areas show peak-normalized mean ± SEM responses across type 5i bipolar cells (n= 8) and type 6 bipolar cells (n= 5). (F) Quantification of step response kinetics. Time to peak and steady-state response amplitude were not different between type 5i and type 6 bipolar cells (p= 0.72 and p= 0.35, respectively; Wilcoxon rank sum test).*

Bipolar cell light responses differ minimally across types

Are transient versus sustained signals already differentiated in the voltage responses of the different bipolar cells presynaptic to ON-T and ON-S RGCs? Or is the distinct excitatory synaptic input that these RGCs receive primarily due to differences at the bipolar cell to RGC synapse? To answer these questions, we compared the light-driven response properties of the bipolar cell subtypes that comprise most of the excitatory input to ON-T or ON-S RGCs. We made targeted electrophysiological recordings from type 5i, type 6 and type 7 bipolar cells in retinal slices from three transgenic mouse lines in which these different bipolar cell subtypes express fluorescent proteins (see Methods). In these experiments, we used somatic whole-cell perforated-patch recordings to limit perturbation of the G-protein signaling cascade that mediates ON bipolar cell light responses.

Somatic resting membrane potentials did not differ significantly among these bipolar cell types (mean ± S.D. V_{rest}: -38 ± 6.3 mV in type 5i (n= 11); -33.7 ± 6.3 mV in type 6 (n= 7); - 36.5 ± 4.7 mV in type 7 (n=6); Kruskal-Wallis test, p= 0.35; values are not corrected for the liquid junction potential since that is hard to estimate in perforated-patch recordings). We characterized light responses using the same spatially-uniform Gaussian noise stimulus (Fig. 4B) and linear-nonlinear model analysis (Fig. 4C and Fig. S7) as in RGC recordings to facilitate direct comparison of results from bipolar cells and RGCs (Kim and Rieke, 2001; Rieke, 2001). LN models of bipolar cell responses accurately predicted responses to noise stimuli (correlation coefficient between average response to repeated noise stimulus and LN model prediction = 0.75 ± 0.15 for n = 18 bipolar cells (n = 13 type 5; n = 3 type 6; n = 2 type 7)). Unlike for ON-T and ON-S RGCs, temporal characteristics of type 5i, type 6 and type 7 bipolar cell linear filters were indistinguishable from each other under our recording conditions (Fig 4B-D). Although there was some variability in the temporal response properties across the population of bipolar cells we recorded, these differences were not associated with morphologically and molecularly defined bipolar cell types. Rather, we observed variability in response kinetics within each bipolar cell subtype and temporal responses thus overlapped substantially across different type 5i, type 6 and type 7 bipolar cells (Fig. 4 and Fig. S7).

Responses to light steps measured in a subset of type 5i and type 6 bipolar cell recordings confirmed our conclusion from Gaussian noise stimuli that different bipolar cell types exhibit nearly identical light response kinetics under our recording conditions (Fig. 4E-F). Unlike the clear differences in light step-evoked excitatory currents we measured in ON-T and ON-S RGCs (Fig. 2D-E), type 5i and type 6 bipolar cells both had sustained responses to light steps. These findings indicate that mechanisms upstream of the generation of the cone bipolar cell voltage response, such as synaptic transmission from cones to cone bipolar cells and intrinsic response properties of the cone bipolar cells, cannot explain the kinetically distinct responses in parallel ON channels mediated by type 5i, type 6 or type 7 bipolar cells. Consistent with this conclusion, ON-T and ON-S RGCs exhibit kinetically distinct light step-evoked spiking responses under scotopic conditions (not shown), where much of the RGC response originates from signals carried from outer to inner retina via the rod bipolar cell pathway (Fig. 1B) (Grimes et al., 2014; Ke et al., 2014). Because AII amacrine cells distribute rod bipolar cell signals directly to cone bipolar cell axon terminals, differences observed under scotopic conditions likely arise at and/or downstream of cone bipolar cell synaptic output.

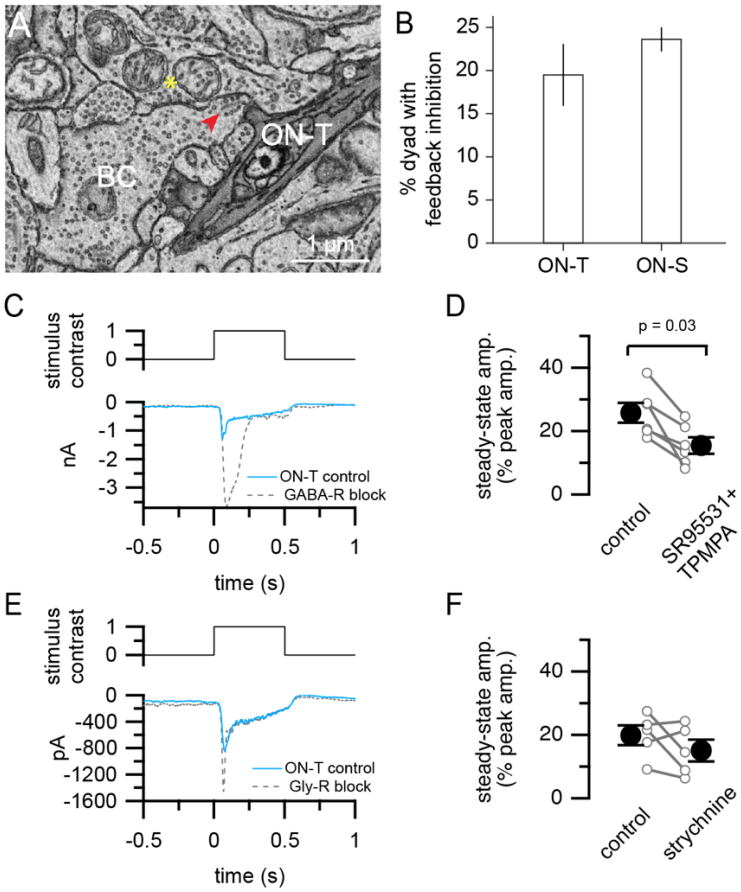

***Figure 5**. Presynaptic inhibition is not required for kinetic differences between bipolar cell inputs to ON-T versus ON-S RGCs. (A) Example EM micrograph showing a ribbon dyad (red arrowhead) between a BC and an ON-T RGC and an amacrine cell, with an adjacent feedback inhibitory synapse (yellow asterisk). (B) Bar plots showing the percentage of RGC/AC ribbon dyads with feedback inhibition. Mean ± SD (n=2 ON-S RGCs 85 dyads analyzed, 2 ON-T RGCs with 83 dyads analyzed) (C) Excitatory currents measured in response to light step increment in control conditions (cyan) and in the presence of GABA receptor antagonists (10 µM SR95531 and 50 µM TPMPA; dashed gray) in an example ON-T RGC. Traces are mean response from six repeats of stimulus presentation. (D) Summary of steady-state amplitudes measured from step responses in control or with GABA receptor antagonists. Step-evoked currents were significantly more transient when $GABA_{A/C}$ receptors were blocked (p= 0.031; Wilcoxon signed rank test; n= 6 RGCs) (E) Control excitatory currents (cyan) or with addition of strychnine (1 µM; dashed gray) to bath in an example ON-T RGC. (F) Summary of strychnine experiments. No significant difference between conditions (p= 0.44; Wilcoxon signed rank test; n= 5 RGCs). In (D) and (F), open circles with lines show measurements from individual ON-T RGCs. Filled circles with error bars show mean ± SEM.*

392 *Presynaptic inhibition does not establish kinetic differences in bipolar cell-mediated excitation*
393
394 Bipolar cells participate in diverse inhibitory circuits with amacrine cells, which are comprised of
395 >40 morphologically and functionally distinct cell types (Diamond, 2017; Helmstaedter et al.,
396 2013). Past work suggests that amacrine cell-mediated presynaptic inhibition is critical to
397 bipolar cell subtype-specific patterns of light-evoked glutamate release (Franke et al., 2017).
398 Our bipolar cell voltage recordings, which should reflect a combination of light-evoked excitatory
399 and inhibitory input, argue that presynaptic inhibition is not required for generating differential
400 synaptic output between type 5i, type 6 and type 7 bipolar cells. However, the slicing procedure
401 we used to prepare tissue for bipolar cell recordings may damage some inhibitory connections,
402 especially long-range amacrine cell inputs. Distance-dependent attenuation of voltage signals
403 between bipolar cell axon terminals and the somatic recording site could also limit our ability to
404 accurately measure the influence of presynaptic inhibition in these recordings. We therefore
405 performed additional anatomical and pharmacological experiments to investigate a possible role
406 for presynaptic inhibition in generating kinetically distinct excitation to ON-T and ON-S RGCs.
407 Many bipolar cell output synapses are organized into a "dyad" arrangement in which a bipolar
408 cell ribbon synapse releases glutamate onto the processes of two different postsynaptic cells. At
409 dyads, bipolar cell output synapses can be presynaptic to the processes of two amacrine cells,
410 two RGCs, or an amacrine cell and a RGC (Cohen and Sterling, 1990; Dowling and Boycott,
411 1966; McGuire et al., 1984; Yu et al., 2023). Dyad synapses comprised of an amacrine cell and
412 a RGC may shape bipolar cell glutamate release dynamics onto the RGC partner because
413 glutamatergic excitation of the postsynaptic amacrine cell can elicit release of inhibitory
414 neurotransmitters (GABA or glycine) from the amacrine cell processes that feed back onto the
415 bipolar cell axon terminal. This form of inhibitory feedback control of bipolar cell output, termed
416 reciprocal inhibition, could potentially contribute to differences in glutamate release onto ON-T
417 and ON-S RGCs.
418
419 We analyzed bipolar cell dyads with postsynaptic amacrine cell processes and either ON-T or
420 ON-S RGC dendrites in SBFSEM volumes to examine whether reciprocal inhibition is likely to
421 generate more transient glutamate release onto ON-T RGCs. We defined putative reciprocal
422 synapses as bipolar cell/amacrine cell/RGC dyads in which we observed clustered vesicles
423 within the amacrine cell process that were in close proximity to the bipolar cell ribbon synapse
424 (Fig. 5A). Our ultrastructural analysis revealed that the prevalence of reciprocal synapses was
425 similar at dyad synapses with postsynaptic ON-T versus ON-S RGCs (Fig. 5A-B). This finding is
426 not consistent with an important role for feedback/reciprocal inhibition in generating differential
427 bipolar cell output onto the different RGC types.
428
429 We also performed pharmacological experiments to further examine what role, if any, inhibition
430 may have in establishing transient glutamate release onto ON-T RGC dendrites. We used
431 ACSF in place of Ames solution for the dissection and maintenance of tissue for these
432 experiments. ACSF is often used in retina experiments, including the glutamate release
433 measurements describe below, and we wanted to check that our results generalized across
434 conditions. Light step-evoked currents in both ON-T and ON-S RGCs were more sustained than
435 responses measured using Ames' solution (Fig. S9A-B). Nonetheless, the difference between
436 sustained and transient RGC types was maintained across different experimental conditions.
437
438 In ON-T RGCs, blockade of $GABA_A$ and $GABA_C$ receptors via bath co-application of SR95531
439 and TPMPA enhanced the peak amplitude of the initial transient component of light-step evoked
440 excitatory synaptic currents (-2023 ± pA 372.7; mean ± S.D.) compared to control (-833.6 ±
441 103.2 pA) (p= 0.031, Wilcoxon sign rank test; n= 6) whereas the sustained component at the

end of the light step was not significantly affected (control: -200.7 ± 14.71 pA; GABA-R block: -290.9 ± 43.69; p = 0.16, Wilcoxon sign rank test; n= 6) (Fig. 5C). The strong enhancement of the initial phase of the response we observed is consistent with prior work showing that $GABA_C$ receptor-mediated inhibition limits multivesicular release from bipolar cells (Sagdullaev et al., 2006). Block of GABA receptors thus made excitatory currents in ON-T RGCs more transient compared to control conditions (Fig 5D). Note that this is opposite the expected effect if presynaptic GABA receptors contribute to generating transient responses in these cells; GABA receptor antagonists should have made excitatory currents more sustained if presynaptic GABAergic inhibition was generating transient bipolar cell input to ON-T RGCs. Thus, GABAergic inhibition appears to control response gain and time course of bipolar cell synaptic output to ON-T RGCs but is not responsible for the transient kinetics of excitatory input to these cells.

We also found that glycinergic inhibition is not likely to contribute importantly to the more transient glutamate release from bipolar cells presynaptic to ON-T RGCs; bath application of the glycine receptor antagonist strychnine did not significantly alter the kinetics of light step-evoked excitatory currents in these cells (Fig. 5E-F). Taken together with our ultrastructural analysis, these results show that amacrine cell-mediated GABAergic or glycinergic inhibition of bipolar cell axon terminals does not explain kinetic differences in excitatory synaptic input to ON-T and ON-S RGCs.

Bipolar cell glutamate release differs across types

Taken together, the bipolar cell and RGC recordings in Figures 2 and 4 indicate that bipolar cell synapses have a key role in the separation of visual signals into transient or sustained channels within ON pathways in the retina. Presynaptic and/or postsynaptic mechanisms could contribute to the distinct kinetics of bipolar cell-mediated excitatory input to ON-T and ON-S RGCs. To investigate whether presynaptic differences in glutamate release from bipolar cell axon terminals shape RGC response kinetics, we expressed the fluorescent glutamate reporter iGluSnFR on the dendrites of ON-T and ON-S RGCs (see Methods). Using two-photon glutamate sensor imaging, we found that light-evoked glutamate signals had significantly faster kinetics at ON-T RGC dendrites (steady-state amplitude as % of peak amplitude = 21 ± 13; mean ± S.D.; n = 224 ROIs) compared to ON-S RGC dendrites (steady-state amp. as % of peak amp. = 44 ± 12; mean ± S.D.; n = 307 ROIs) (Fig. 6).

The experiments summarized in Figure 5 suggest that presynaptic inhibitory input to bipolar axon terminals is not required for the difference between ON-T and ON-S responses. The glutamate release measurements provided a further test. We compared the kinetics of release before and after suppressing spiking amacrine cell activity (with bath application of the voltage-gated Na^+ channel blocker TTX) or all amacrine cells (with bath application of the glutamate receptor antagonist NBQX). This approach avoided the confounding changes in excitatory signals we encountered with inhibitory receptor blockers (e.g. the increase in excitatory input to ON-T RGCs in Figure 5C and oscillatory bursts of excitation in ON-S RGCs (not shown)). The more transient glutamate release kinetics at ON-T vs ON-S dendrites remained even when amacrine cell responses were suppressed (control: steady-state amp. as % of peak amp. 13 ±10; mean ± S.D.; n = 189 ROIs/4 FOVs for ON-T dendrites vs. 40 ± 12; mean ± S.D.; n = 287 ROIs/8 FOVs for ON-S dendrites; TTX: 16 ± 9; mean ± S.D.; n = 50 ROIs/3 FOVs for ON-T dendrites vs. 35 ± 11; mean ± S.D.; n = 146 ROIs/6 FOVs for ON-S dendrites; *p<0.001; t-test); NBQX: 7 ± 3; mean ± S.D.; n = 112 ROIs/1 FOV for ON-T dendrites vs 24 ± 9; mean ± S.D.; n = 97 ROIs/2 FOVs for ON-S dendrites; *p<;0.001; t-test; Figure 7).

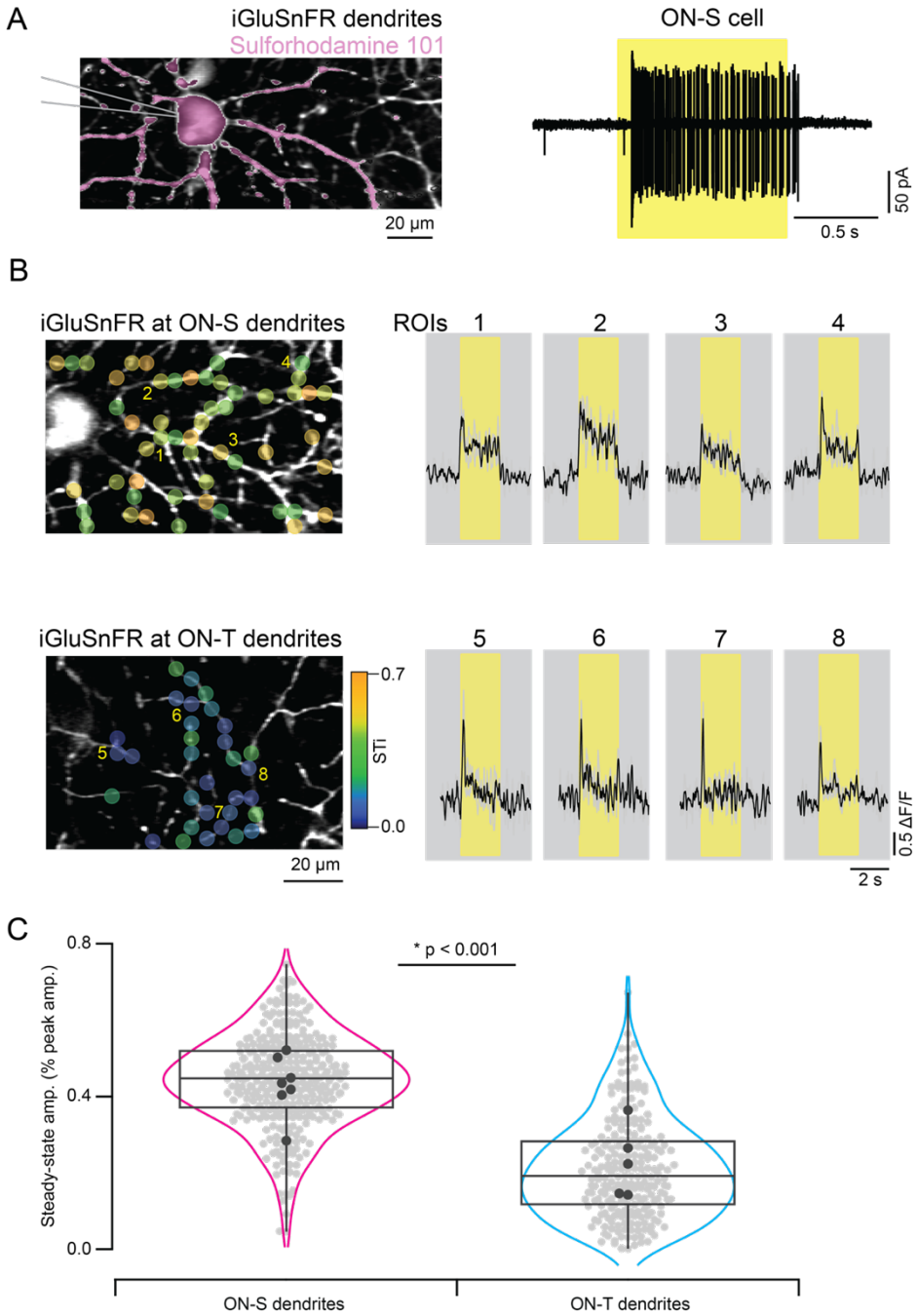

***Figure 6**. Distinct glutamate input kinetics at ON-S vs ON-T RGC dendrites. (A) ON-S RGC dendrites expressing iGluSnFR in a Kcng4-Cre mouse were filled with sulforhodamine 101 (left) after measuring their spiking response to a 200 µm spot extracellularly (Right). Yellow bands indicate stimulus duration. (B) iGluSnFR expressing ON-S and ON-T dendrites at different depths of the inner-plexiform layer (Left) were imaged using two-photon microscopy. Example iGluSnFR signals extracted from small regions of interest (ROIs 1-8) from ON-S and ON-T RGC dendrites illustrate the kinetic differences in their respective inputs. Black, mean responses; gray, individual trials. (C) Distribution of steady-state response amplitudes (mean fluorescence during last 1 s of stimulus) of the individual (gray) and average (black) ROIs from ON-S and ON-T dendrites evoked by a 200 µm static spot (n = 7 FOVs, 6 retinas for ON-S and 5 FOVs, 5 retinas for ON-T RGC dendrites, *p<0.001; t-test beween ROIs).*

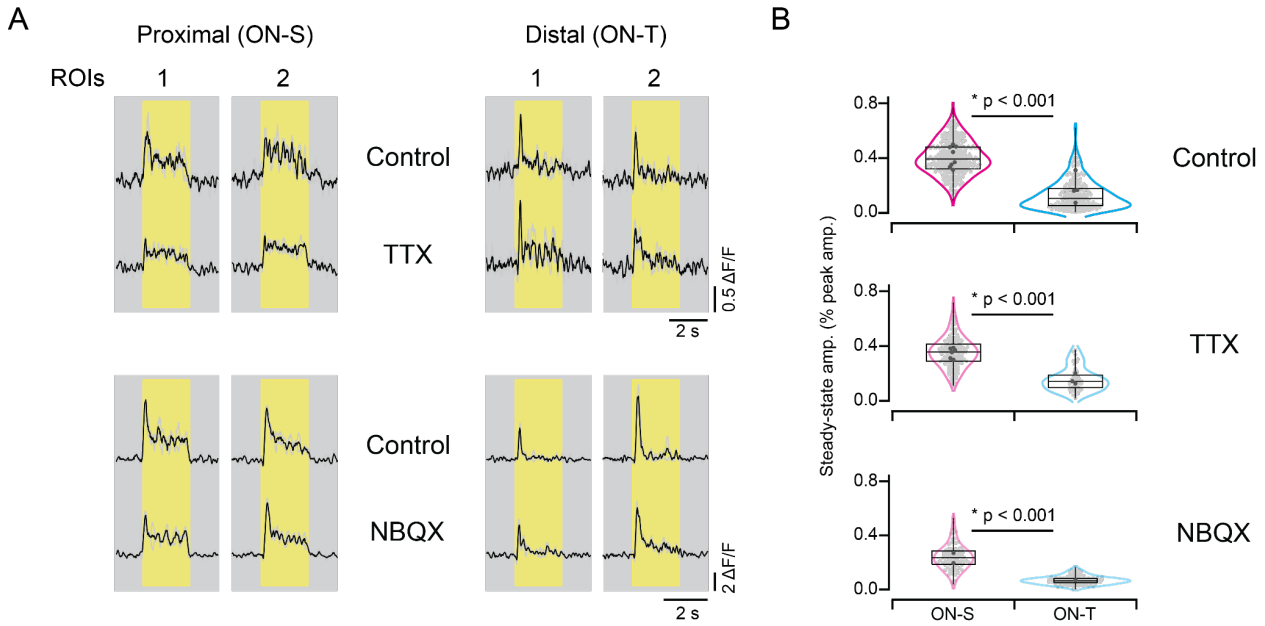

***Figure 7**. Distinction between sustained and transient responses remains when amacrine cell activity is blocked. A. iGluSnFR measurements of glutamate release in control conditions and in the presence of TTX (which blocks spike-dependent amacrine cell output); or in the presence of NBQX, which blocks AMPA receptor mediated input to all amacrine cells (as well as horizontal cells). B. Ratio of steady state to transient response across ROIs before (top) and during (bottom) application of TTX/NBQX.*

These results show that differences in glutamate release from presynaptic bipolar cells contribute to transient versus sustained ON RGC responses and that the differences in release are retained without amacrine feedback to bipolar cells. These experiments do not, however, rule out the possibility that additional postsynaptic mechanisms, for example differential glutamate receptor expression, contribute to kinetic differences between RGC types.

Although whole-cell excitatory currents in ON-T and ON-S RGCs (Fig. 2, Fig. S8) and iGluSnFR signals measured from ON-T and ON-S RGC dendrites (Fig. 6) both exhibited clear kinetic differences between the RGC types, there were quantitative differences in the response to light steps between the different measurement approaches. As described above, these differences appear to arise from differences in the external solution (Ames vs ACSF). The iGluSnFR experiments used an ACSF solution, like the patch-clamp experiments in Figs. 5 and S8. Both iGluSnFR responses and excitatory synaptic inputs measured in ACSF showed a larger sustained component of the step response at both ON-T and ON-S dendrites compared to currents measured in Ames (compare Fig. 2D-E, Fig. S8A-B and Fig. 6B-C). This observation highlights the importance of comparing responses between different RGC types, as well as between RGCs and bipolar cells, under identical recording conditions.

Importantly, the kinetics of glutamate release measured using iGluSnFR resemble the excitatory synaptic inputs to ON-T and ON-S RGCs more closely than the relevant bipolar voltage responses (Fig. 4). This indicates that the difference between the ON-T and ON-S responses originates at least in part in the conversion of bipolar voltage to glutamate release.

Ribbon size and vesicle replenishment

Prior work has shown that bipolar cells can exhibit profound short-term depression of glutamate release due to use-dependent depletion of the readily-releasable pool of synaptic vesicles (Burrone and Lagnado, 2000; Singer and Diamond, 2006, 2003; von Gersdorff and Matthews, 1997). Strong vesicle depletion at the cone bipolar cell synapses onto ON-T RGCs could generate more transient responses in these cells compared to ON-S RGCs. To examine this possibility, we measured excitatory synaptic inputs to ON-T and ON-S RGCs in response to a paired flash stimulus in which two brief light flashes were separated by varying time intervals. As in Figures 1, 2 and 4, we used Ames' medium for tissue preparation and maintenance in these experiments. These experiments used the same photopic background light level (~3300 R*/rod/s; ~2000 P*/Scone/s; ~1650 P*/Mcone/s) as used for Gaussian noise and step stimuli.

Flash-evoked excitatory synaptic currents were suppressed in both RGC types at short inter-flash intervals, consistent with incomplete recovery from vesicle depletion at the time of the second flash (Fig. 8A top/middle, B). This suppression was much stronger for currents measured in ON-T RGCs compared to ON-S RGCs. We quantified the extent of suppression using a paired flash ratio, which was calculated as the peak amplitude of the response to the second flash divided by the peak amplitude of the response to the first flash. At the shortest interval we tested (50 ms), the response to a second flash was almost completely suppressed in ON-T RGCs (paired flash ratio = 0.04 ± 0.03; mean ± S.D.; n = 6) whereas the response to a second flash in ON-S RGCs was suppressed considerably less (paired flash ratio = 0.29 ± 0.08; n = 5). To rule out the possibility that a reduction in bipolar cell voltage response to the second flash could account for the strong paired flash suppression of excitatory input to RGCs, we also measured type 5i bipolar cell responses to the paired flash stimuli. The amplitude of flash-evoked voltage responses in type 5i bipolar cells was unchanged by a preceding flash at all time intervals (Fig. 8A bottom, C), which argues that paired flash suppression arises at the bipolar output synapse. These results are consistent with the idea that differences in the extent of stimulus-evoked vesicle pool depletion in bipolar cells could underlie transient versus sustained excitatory input to ON-T and ON-S RGCs.

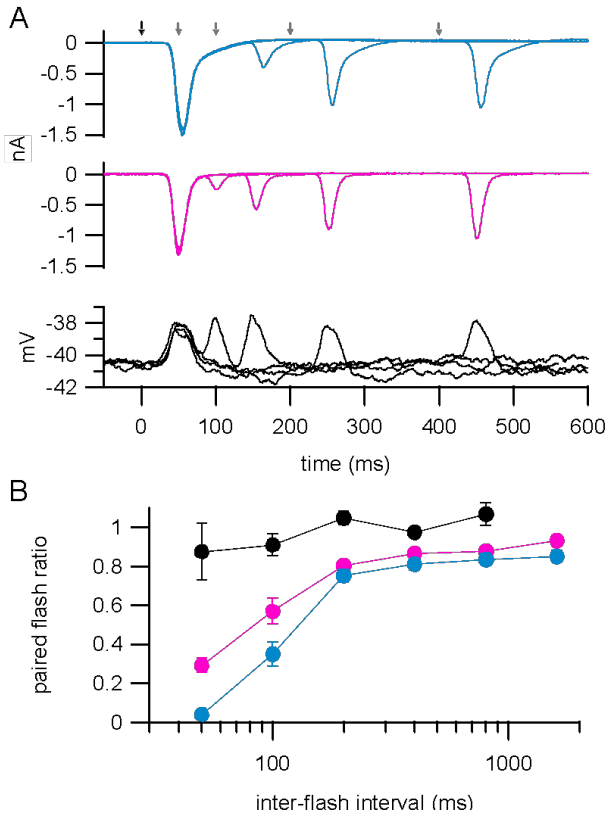

Figure 8. *Stronger flash-evoked suppression of excitatory currents in ON-T versus ON-S RGCs. (A) Paired flash-evoked excitatory currents measured at different inter-flash intervals (50, 100, 200, 400 ms) in an example ON-T (top; cyan) and an ON-S (middle, magenta) RGC. Bottom black traces show voltage responses to same stimulus measured in an example type 5i bipolar cell. Arrows at top indicate timing of first flash (black) and second flashes (gray). Flashes were 400% contrast and 10 ms duration. Traces show mean responses to five repeats of each paired flash interval. (B) Filled circles with error bars show mean ± SEM paired-flash ratios at different inter-flash intervals across all ON-T RGCs (cyan; n= 6), ON-S RGCs (magenta; n= 5) and type 5i bipolar cells (black; n= 6).*

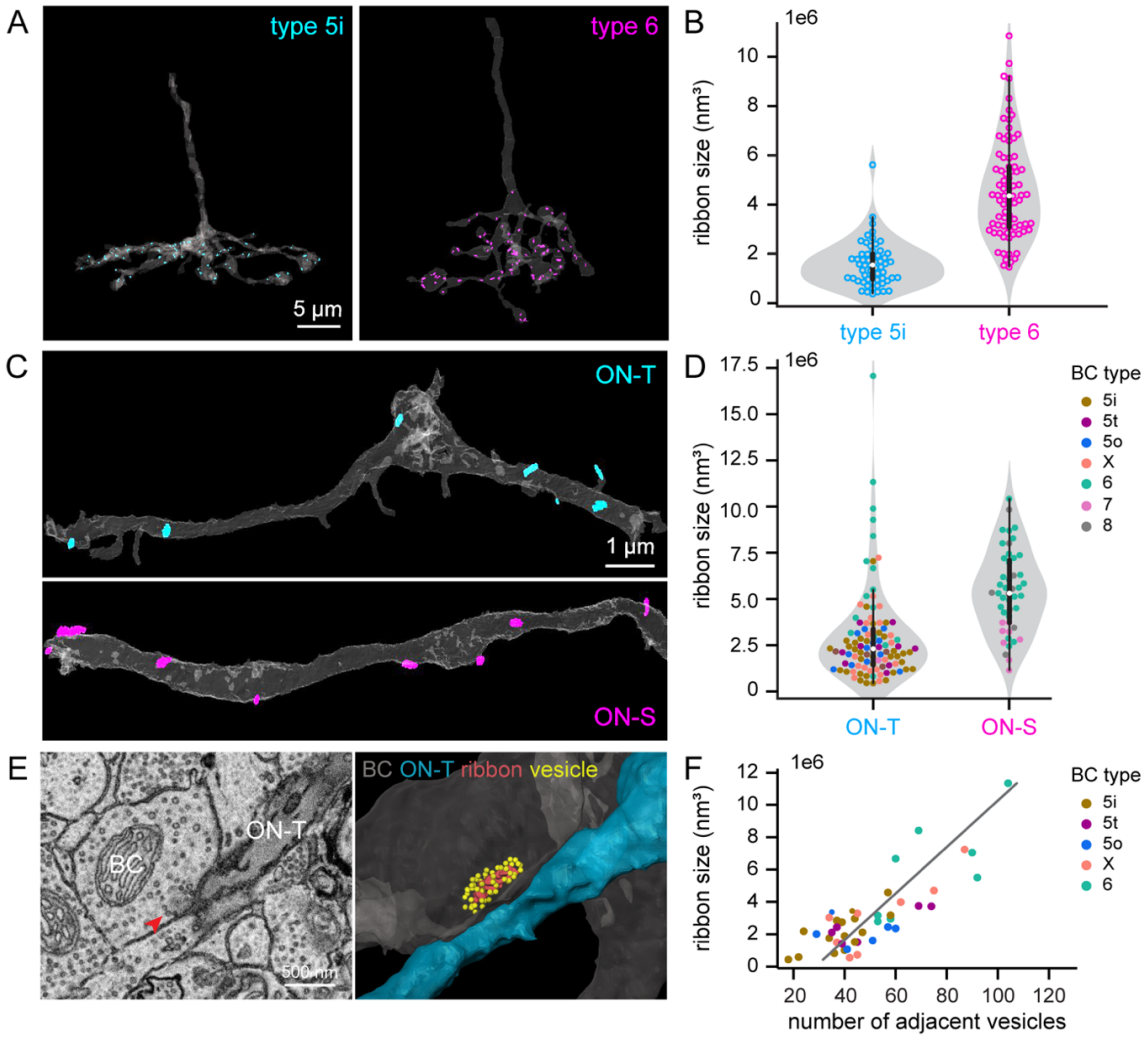

Figure 9. *Bipolar cell subtype-specific differences in ribbon size (volume). (A) 3D reconstructions showing segmented axon stalk and axonal terminal (gray) and all the synaptic ribbons within the axonal terminal for a type 5i (cyan) and a type 6 (magenta) BC. (B) Violin plot showing distribution of ribbon volumes (each data point is a ribbon) for the type 5i and type 6 BC in (A). The boxes indicate the interquartile range (thick lines, 25%-75%), median value (white dot), and 1.5 times interquartile range (thin line). Shaded gray areas represent rotated kernel density plots. (C) 3D reconstructions showing segmented dendritic arbor (gray) and all the synaptic ribbons presynaptic to these segments of ON-T (cyan) or ON-S (magenta) RGC dendrites. (D) Violin plot with scattered dots showing ribbon volumes for each ribbon presynaptic to a stretch of reconstructed ON-T or ON-S RGC dendrite. Each ribbon (dot) is colored differently for each BC type. (E) An EM micrograph (left) and 3D reconstruction (right) of a ribbon and its adjacent vesicles. The ribbon is indicated by the red arrow in the EM image. In the 3D reconstruction, yellow dots indicate the adjacent vesicles surrounding the presynaptic ribbon (red) in the BC terminals (gray). Postsynaptic ON-T RGC is in blue. (F) Scatter plot showing ribbon size in volume in relationship with the number of adjacent vesicles. Gray line represents the linear regression model fitted to the data. Linear regression:* $\beta = 6.98e{-}06$, $p < 0.001$, $r^2 = 0.66$.

We next looked for ultrastructural correlates of differential synapse function in bipolar cell axon terminals reconstructed from SBFSEM volumes. Interestingly, type 6 bipolar cell synaptic ribbons were ~2-3 fold larger than those of types 5i bipolar cells (Fig. 9A-B, Fig. S10A). These differences did not depend on the identity of the postsynaptic RGC partner (Fig. 9D, Fig. S10B). Ribbons in XBCs, type 5o and type 5t bipolar cells were also smaller than type 6 bipolar cell ribbons (Fig. 9D, Fig. S10B). This bipolar cell subtype-specific difference in ribbon size and the difference in ratio of type 6 to type 5i input between RGC types meant that ribbons were on average smaller at synapses made on ON-T compared to ON-S dendrites (Fig. 9C-D, Fig. S10B).

Discussion

We sought to understand how kinetically distinct visual pathways are established in the retina by directly comparing the visual response properties of transient and sustained ON RGCs with their presynaptic bipolar cells. Our results show that bipolar cell synapses have a key role in establishing different temporal channels in ON circuits of the retina. Further, amacrine cell-mediated presynaptic inhibition does not appear to account for transient versus sustained bipolar cell synaptic output. Rather, bipolar cell subtype-specific differences in synaptic release properties likely generate kinetically distinct output to postsynaptic targets. Our anatomical analysis suggests that these differences may at least in part be due to differences in synaptic vesicle pool size.

A key aspect of our work is that we measured RGC and bipolar cell responses using identical stimuli and under the same experimental recording conditions. To our knowledge, a direct comparison of RGC responses with those of their presynaptic bipolar cells has not previously been reported. The importance of measuring RGC and bipolar cell responses under the same conditions is highlighted by our observation that excitatory synaptic currents measured in ON alpha RGCs exhibited quantitatively different kinetics, although relative differences between types were preserved, when measurements were made from retinas maintained in ACSF versus Ames' bath solution (compare Fig. 2 (Ames') and Figs. 5 and S9 (ACSF)).

We found that the bipolar cell subtypes that provide the major input to ON-T (type 5i) or ON-S RGCs (types 6 and 7) had indistinguishable light-evoked voltage responses (Figure 4). This was not entirely surprising given that most or all ON cone bipolar cell subtypes are indirectly coupled to other nearby ON cone bipolar cells via electrical synapses between bipolar cell axon terminals and the distal processes of AII amacrine cells. These electrical synapses form the basis for the primary rod pathway that mediates vision under dim light conditions, but lateral signals can also flow among neighboring bipolar cells under conditions where cone signaling dominates (Demb and Singer, 2012). Indeed, a substantial fraction (~30-50%) of light-evoked responses in the bipolar cell types we investigated here can be attributed to lateral signals that arrive via electrical synapses at photopic light levels (Kuo et al., 2016). Each AII amacrine cell is electrically coupled to multiple ON cone bipolar subtypes as well as to other AII amacrine cells (Marc et al., 2014; Tsukamoto and Omi, 2017; Veruki and Hartveit, 2002a, 2002b). Different ON cone bipolar cell subtypes may also be directly coupled via gap junctions to each other (Sigulinsky et al., 2020; Tsukamoto and Omi, 2017).

Direct or indirect (via AII) coupling may limit the extent to which different bipolar cells can generate subtype-specific voltage responses. These findings differ from a previous study that found some differences among mouse ON cone bipolar cell subtypes. Ichinose et al., (2014) reported that a subset of type 5 bipolar cells, which the authors termed type 5f, and type 7

bipolar cells had more transient responses than type 6 bipolar cells. Methodological differences may account for the discrepancy between our results and the previous work by Ichinose et al., (2014). For example, Ichinose et al. included inhibitory receptor antagonists in their experimental solutions and used 100 µm diameter spots to characterize bipolar cell responses whereas we left inhibitory signaling intact and used larger (520 µm diameter) spots to match the stimuli we used for RGC recordings. Interestingly, a recent investigation of spatial and temporal response properties of light-evoked intracellular calcium signals across bipolar cell types suggests that ON bipolar cells can exhibit type-specific response kinetics for small stimuli (<~200 µm diameter) but not larger spot sizes, presumably due to surround inhibition (Hsiang et al., 2024). Regardless of the reasons for the different findings, our observation that bipolar cell subtypes exhibited similar responses under the same recording and light stimulus conditions for which we observed obvious differences among postsynaptic RGCs argues that mechanisms upstream of bipolar cell glutamate release (e.g. cone to bipolar cell synapses or intrinsic voltage response properties of bipolar cells) are unlikely to have a major role in shaping RGC type-specific responses for the stimuli we used here.

A limitation of our work is that we did not record from every one of the bipolar cell subtypes that are presynaptic to ON-T RGCs. Instead, we measured responses from type 5i and type 6 bipolar cells, which together comprise >~50% of the synaptic input to ON-T RGC dendrites. It is possible that the other presynaptic bipolar cell types (type 5o, type 5t and XBC) may have more transient light-evoked voltage responses that could contribute to the transient excitation measured in ON-T RGCs. In fact, a previous study in mouse retina found that XBCs and a subset of type 5 bipolar cells express voltage-gated Na^+ channels (Hellmer et al., 2016). These channels may enhance response transience or might even contribute to the generation of light-driven all-or-none spiking responses in these bipolar cells (Ichinose et al., 2014; Puthussery et al., 2013; Saszik and DeVries, 2012).

Even if transient intrinsic response properties of type 5o, 5t and XBC bipolar cells contribute to the generation of transient responses in ON-T RGCS, this alone is unlikely to account for the kinetics of the excitatory synaptic currents we measured in these RGCs. Type 5i and type 6 bipolar cells have a significant sustained component of their light step-evoked voltage response (Fig. 4E-F), whereas excitatory currents measured for the same stimulus and under the same conditions in ON-T RGCs had little to no sustained component (Fig. 2D-E). We would expect to observe some sustained excitatory input to ON-T RGCs if type 5i and type 6 bipolar cell synaptic output follows the voltage response of these bipolar cells. Thus, a marked transformation of the sustained bipolar cell membrane voltage response to a transient synaptic current must take place. Our measurements of extracellular glutamate at ON-T and ON-S dendrites (Fig. 5) suggest that much of this transformation occurs at the level of bipolar cell glutamate release. It is interesting in this context that ON-T and ON-S RGCs both receive input from type 6 bipolar cells (comprising ~20% and ~50% of total synaptic input, respectively). Due to differences in dendrite stratification, type 6 bipolar cell synapses onto ON-T RGCs arise from a region of the axon that is located more proximal to the bipolar cell soma than the synapses formed onto ON-S RGCs, which are found within the distal axon lobules. However, we did not observe any differences in ribbon size at distal versus proximal locations in type 6 bipolar cell axons (Figure 9D). Whether postsynaptic target-specific synapse function, as has previously been reported in salamander retinal bipolar cells (Asari and Meister, 2014, 2012) and mouse starburst amacrine cells (Pottackal et al., 2021), contributes to signal diversification in circuits involving type 6 bipolar cells will require further investigation.

Our electrophysiological and glutamate imaging results indicate that amacrine cell-mediated inhibition at bipolar cell synaptic terminals is not necessary for generating transient glutamate release kinetics onto ON-T RGC dendrites. This is seemingly at odds with prior work that has indicated an essential role for surround inhibition in establishing type-specific bipolar cell glutamate release dynamics (Franke et al., 2017). However, we note that our analysis here focused only on whether presynaptic inhibition shapes the kinetics of excitatory inputs to ON-T RGCs. Our anatomical and pharmacological experiments together argue that presynaptic inhibition is not an important factor in the transformation from sustained bipolar cell voltage responses to transient excitatory synaptic currents in ON-T RGCs. This is not to say that amacrine cell-mediated inhibition does not have a role in generating subtype-specific response properties for other aspects of bipolar cell function. Indeed, inhibition does have an important role in establishing differential spatial tuning of excitatory inputs to the RGC types we studied; excitatory synaptic currents in ON-T RGCs exhibit stronger surround inhibition than ON-S RGCs, and this surround inhibition is reduced by bath application of GABA receptor antagonists (Fig. S9C). Interestingly, recent work revealed postsynaptic target-specific surround inhibition at neighboring type 6 bipolar cell output synapses within the same axon terminal (Swygart et al., 2024). Whether target-specific presynaptic inhibition of type 6 bipolar cells also contributes to differential surround inhibition between ON-T and ON-S RGCs or is primarily due to differences across bipolar cell types (e.g. type 5i/5t/XBC vs. type 6/7), remains to be determined.

We conclude that transient versus sustained excitatory inputs to ON-T and ON-S RGCs most likely arise from bipolar cell subtype-specific differences in synaptic release properties. Excitatory inputs to ON-T RGCs exhibited stronger paired flash depression than those to ON-S RGCs (Fig. 8), which indicates distinct vesicle cycling dynamics at the bipolar cell axon terminals presynaptic to the different RGC types. Our ultrastructural analysis suggests that bipolar subtype-dependent differences in ribbon size may be a factor in establishing transient versus sustained glutamate release kinetics (Fig. 9). It is important to note, however, that type 7 bipolar cells (~45% of excitatory input to ON-S RGCs) have small synaptic ribbons, yet iGluSnFR imaging of type 7 bipolar cell axon terminals found that these cells exhibit sustained glutamate release (Srivastava et al., 2022).

We found that ribbon size is strongly correlated with the total number of vesicles that are in close contact with the synaptic ribbon across different ON bipolar cell types (Fig. 9E-F, Fig. S10C). Thus, there are fewer ribbon-associated vesicles at glutamatergic synapses formed on ON-T RGC dendrites compared to those at ON-S RGCs. Ribbon-associated vesicles are thought to correspond to the releasable pool of vesicles, comprised of both a readily-releasable pool that are docked at the base of the ribbon, at the presynaptic active zone, and a reserve (alternatively referred to as ‘releaseable’) pool of vesicles that are bound to the ribbon at more distal sites (Grabner et al., 2023; Lagnado and Schmitz, 2015; von Gersdorff et al., 1996; Wan and Heidelberger, 2011). The number of ribbon-associated vesicles, as well as the rate at which the readily-releasable and reserve vesicle pools are replenished following exocytosis, together define the amplitude and time course of stimulus-evoked vesicle release (Jackman et al., 2009; Lagnado and Schmitz, 2015; Neves and Lagnado, 1999; Oesch and Diamond, 2011; Singer and Diamond, 2006; von Gersdorff and Matthews, 1997). For example, a small pool of readily-releasable vesicles and relatively slow replenishment in rod bipolar cell axon terminals contributes to transient release kinetics from these cells (Singer and Diamond, 2006). Our observation that the average excitatory synaptic input to ON-T RGCs is smaller and that most excitatory input to ON-T cells originates from bipolar synapses with fewer ribbon-associated vesicles are consistent with a role for vesicle depletion in establishing transient glutamate release onto these RGCs. The larger pool of ribbon-associated vesicles in type 6 bipolar cell

terminals, which comprise ~ 55% of the synaptic input to ON-S RGCs, may support sustained synaptic transmission onto these RGCs. However, additional mechanisms, such as bipolar cell type-specific differences in the rate of refilling of the ribbon-associated vesicles could also contribute to sustained versus transient glutamate release.

Direct measurements of exocytosis at ribbon synapses show that release rates increase with increasing ribbon size and the number of vesicles bound to the ribbon. Evidence for this dependence includes a tight correspondence between functional measures of the releasable vesicle pool and anatomical measurements of the number of vesicles bound to the ribbon (Grabner et al., 2023; von Gersdorff et al., 1996). Ribbon size and the number of ribbon-associated vesicles vary across the day-night cycle; these morphological changes are correlated with diurnal changes in maintained vesicle fusion rates (Babai et al., 2016; Dembla et al., 2020; Hull et al., 2006). Finally, release rates decrease when ribbon size is reduced (Mehta et al., 2013; Wakeham et al., 2023), or when ribbons are ablated either abruptly or genetically (Grabner and Moser, 2021; Maxeiner et al., 2016; Mehta et al., 2013; Snellman et al., 2011). These biophysical studies are consistent with the correlation that we observe here between ribbon size and the extent to which transmitter release is transient vs. sustained. A note of caution in making this comparison is that exocytosis is sensitive to the voltage trajectory (Snellman et al., 2009), and the biophysical studies often use more rapid and larger voltage changes than those elicited by physiological light inputs. In fact, genetic deletion of ribbons does not strongly alter light-evoked excitatory currents in ON-S RGCs (Okawa et al., 2019). Why ribbon deletion has relatively little effect on light-evoked responses in ON-S RGCs remains to be determined. It is interesting to note that ~30% of synapses formed by type 6 bipolar cells onto ON-S RGC dendrites lack ribbons even in wildtype retina (Okawa et al., 2019). Future studies will be needed to investigate to what extent such ribbonless synapses could contribute to bipolar cell type-specific differences in glutamate release such as we observed here.

The dynamics of transmitter release are also impacted by vesicle depletion and the time required for refilling of releasable vesicle pools following strong stimulation. In particular, the sustained transmitter release rate should be equal to the sustained refilling rate. Direct measurements of refilling at the cone output synapse following strong activation show that it is quite slow – with a time constant near 1 sec (Grabner et al., 2016; Jackman et al., 2009; Rabl et al., 2006). This is far too slow to explain the recovery from paired-flash depression that we observe here. Several factors may contribute to this difference. First, postsynaptic receptor saturation can contribute to paired-pulse depression, and it can recover from such depression more quickly than presynaptic release (Grabner et al., 2016). Second, the paired-flash depression that we measure in RGC synaptic inputs is largely absent in the bipolar voltage responses. This suggests that it is dominated by a history-dependence at the cone bipolar output synapses and refilling of vesicle pools may proceed more quickly at bipolar synapses than cone synapses.

Mechanisms that we did not directly investigate here may also contribute to the difference between transient and sustained responses. For example, presynaptic resting potential has a strong effect on steady-state vesicle release and thus stimulus-evoked release dynamics. Exocytosis that occurs when bipolar cells rest at voltages near release threshold can lead to a depletion of readily-releasable vesicles that limits the amount of release that occurs upon further light-induced depolarizations (Grimes et al., 2014; Jarsky et al., 2011; Oesch and Diamond, 2011). Thus, an initial phasic component of release can be reduced by depolarized resting potentials whereas hyperpolarized potentials can facilitate greater occupancy of vesicles in the releasable pool, which can enhance response transience. Bipolar subtype-dependent

796 differences in release threshold due to differential Ca^{2+} channel expression/regulation (Pangrsic
797 et al., 2018) and/or coupling between Ca^{2+} channel activity and vesicle release (Burrone et al.,
798 2002; Burrone and Lagnado, 2000) could also impact release dynamics. Several aspects of
799 excitatory synaptic currents in the two RGC types we studied here are consistent with a
800 situation in which bipolar cell inputs to ON-T RGCs have a higher threshold for glutamate
801 release compared to those at ON-S RGCs; ON-T RGCs receive less spontaneous excitatory
802 synaptic input than ON-S RGCs (Kuo et al., 2016) and stimulus-evoked EPSCs are slower,
803 sparser and more biased towards larger amplitude events in ON-T RGCs compared to those in
804 ON-S RGCs (Fig. 2, Fig. S1B). Further investigation will be required to determine whether this is
805 due to differences in axon terminal resting potential and/or other presynaptic factors. We did not
806 find evidence for subtype-specific differences in resting membrane potential among type 5i, type
807 6 and type 7 bipolar cells, but our somatic voltage recordings likely have limited ability to resolve
808 small voltage differences at the bipolar cell axon terminals.
809
810 Our results do not rule out additional roles for postsynaptic mechanisms in establishing transient
811 versus sustained RGC spike output. For example, delayed amacrine cell-mediated inhibitory
812 synaptic input to RGC dendrites could truncate spiking responses (Nirenberg and Meister,
813 1997). We did not observe a significant difference in the light-evoked excitation/inhibition
814 amplitude ratio between ON-S and ON-T RGCs (Fig. S3E), but our data does not exclude a
815 role for postsynaptic inhibition in generating transient responses. RGC cell-intrinsic
816 mechanisms, such as RGC subtype-specific differences in voltage-gated Na^+ channel
817 properties and/or expression pattern could also contribute to distinct response kinetics
818 (Brombas et al., 2022; Chang et al., 2023; Werginz et al., 2020). While a combination of pre-
819 and postsynaptic factors may ultimately act in concert to generate transient versus sustained
820 RGC spike output (Warwick et al., 2018; Werginz et al., 2020), our results establish a
821 fundamental role for bipolar cell synapses in the segregation of visual input into kinetically
822 distinct channels in ON pathways of the retina.
823
824 ***Materials and Methods***
825
826 *Animals*
827
828 Experiments used 5- to 15-week-old wild-type, *Grm6-tdTomato* (Morgan et al., 2011), *Gus8.4-*
829 *EGFP* (Huang et al., 1999), *Gjd2-EGFP*, or Kcng4-Cre (Duan et al., 2014) transgenic mice.
830 Transgenic mouse strains were backcrossed into the same genetic background as wild-type
831 mice (C57BL/6J; Jackson Laboratory). Animal care and handling followed procedures approved
832 by the Institutional Animal Care and Use Committee of the University of Washington or the
833 University of Victoria Animal Care Committee.
834
835 *Tissue preparation*
836
837 Retinal tissue was prepared for physiological recordings as previously described (Kuo et al.,
838 2016; Srivastava et al., 2022). Briefly, mice were killed by cervical dislocation or decapitation
839 and retinas were dissected from both eyes in oxygenated (95% O_2, 5% CO_2), bicarbonate-
840 buffered Ames' (Sigma) or artificial cerebrospinal fluid (ACSF) solution and either flat-mounted
841 with the vitreal surface facing up onto a poly-D-lysine coated glass coverslip (Corning) (RGC
842 patch-clamp recordings and iGluSnFR imaging) or sliced in an orientation perpendicular to the
843 flat-mount plane using a vibratome (200 µm slice thickness; bipolar cell recordings) before being
844 transferred to an upright 2P fluorescence microscope. ACSF contained (in mM): 125 NaCl, 2.5
845 KCl, 1.2 $CaCl_2$, 1.5 $MgCl_2$, 1.25 NaH_2PO_4, 20 glucose, 0.5 L-glutamine, 0.1 sodium ascorbate,
846 and 26 $NaHCO_3$ (pH 7.4, 310mOsm/L). For preparation of retinal slices, isolated retina was

surrounded with melted agarose (maintained at ~40ºC) followed by rapid cooling using an ice block. The embedded retina was then positioned in front of the vibratome blade in an orientation orthogonal to the flat mount plane for sectioning. All experiments exclusively used tissue from ventral retina.

Electrophysiology

During recordings, retinal tissue was continuously perfused (~6-8 mL/min) with oxygenated, bicarbonate-buffered Ames' solution maintained at 30-34 ºC. In a subset of electrophysiological recordings (Figs. 6C-F and S8), tissue was perfused with ACSF rather than Ames' solution. Electrical signals were acquired at 10 kHz and low-pass filtered at 3 kHz using a Multiclamp 700B or Multiclamp 700A amplifier (Molecular Devices) and Symphony Data Acquisition software (http://symphony-das.github.io). The somas of different ON bipolar cell subtypes were targeted for gramicidin perforated-patch current-clamp recordings using 2P laser scanning excitation (960nm) in retinal slices prepared from transgenic mouse lines in which bipolar cell subtypes expressed fluorescent proteins. Tissue from *Grm6-tdTomato* mice, in which a sparse subset of ON bipolar cell types (type 6, 7 and 8) express tdTomato was used to target recordings to type 6 bipolar cells (Morgan et al., 2011; Schwartz et al., 2012). Type 7 bipolar cells were targeted for recording in *Gus8.4-EGFP* mice, which express EGFP in a type 7 bipolar cells and rod bipolar cells (Huang et al., 2003). Type 5i bipolar cells were targeted in retinas from *Gjd2-EGFP* mice, which we found express EGFP selectively in these bipolar cells (Fig. S6) as well as less robustly in an uncharacterized amacrine cell type (not shown). For bipolar cell recordings, we minimized light exposure from the 2P laser by restricting scan regions to the inner retina, away from photoreceptors, and by keeping laser exposure brief (<~30 sec/scan region; <2 mW post-objective laser power) (Kuo et al., 2016). After identification of fluorescent cell bodies, we acquired recordings using infrared differential interference contrast microscopy. Bipolar recordings used an internal solution containing 123 mM K-aspartate, 10 mM KCl, 10 mM HEPES, 1 mM $MgCl_2$, 1 mM $CaCl_2$, 2 mM EGTA, 4 mM Mg-ATP, 0.5 mM Tris-GTP, 100 µM Alexa Fluor 594-hydrazide and 25-30 µg/mL gramicidin D (280 mOsm/L; pH 7.2). Pipettes (~7-9 Ω tip resistance) were front-filled with gramicidin-free internal solution to facilitate formation of high resistance (>1 GΩ) seals between patch pipettes and the cell membrane. After seal formation, series resistance (R_s) was monitored in voltage-clamp mode by applying a 10 mV voltage step across the pipette tip. Experiments were initiated once R_s declined to <50 MΩ, which typically took 20-30 min. During recordings, we occasionally confirmed the integrity of the cell membrane under the recording electrode by monitoring Alexa Fluor 594 fluorescence using 2P excitation; if any dye was visible in the cell body, we abandoned the recording. No holding current was applied during current-clamp recordings from bipolar cells. At the conclusion of each bipolar cell recording, the membrane under the patch pipette was intentionally ruptured and fluorescence images of Alexa Fluor 594-filled cells were acquired using 2P microscopy to confirm bipolar cell subtype identities (Wässle et al., 2009).

RGC recordings were performed in a flat-mount preparation of the retina from wild-type mice or *Gjd2-EGFP* transgenic mice following previously described methods (Kuo et al., 2016). Excitatory synaptic currents were isolated in whole-cell voltage-clamp recordings by holding RGCs near the reversal potential for Cl^-- mediated conductances (-68.5 mV). Patch pipettes (2.5-4 MΩ) were filled with an internal solution containing (in mM): 105 Cs-methanesulfonate, 10 Tetraethylammonium-Cl, 20 HEPES, 10 EGTA, 2 QX-314, 5 Mg-ATP, 0.5 Tris-GTP (~280 mOsm; pH 7.2). Series resistance (<15 MΩ) was compensated by 70% using the amplifier circuitry. Inhibitory receptor antagonists (SR-95531, TPMPA, strychnine) were obtained from Tocris or Sigma Aldrich and added to the bath solution from concentrated aqueous stock solutions.

898
899 *iGluSnFR expression and two-photon imaging*
900
901 Intravitreal injection of a cre-dependent viral vector (pAAV.hSyn.Flex.iGluSnFR.WPRE.SV40;
902 Addgene Catalog #98929-AAV1) was performed into Kcng4-cre mice to selectively express the
903 glutamate sensor, iGluSnFR, in alpha RGCs, including ON-T and ON-S RGCs (Krieger et al.,
904 2017). All injection procedures, tissue preparations, and subsequent two-photon imaging were
905 performed as previously described in Srivastava et al., 2022. Briefly, for iGluSnFR imaging, the
906 laser was tuned to 920 nm and all recordings were acquired at a frame rate of 58.25 Hz (256 x
907 256 pixels). In KCNG4-Cre mice, ON-S alpha RGCs were first identified by their spiking
908 properties using extracellular cell-attached recordings. To identify the dendrites of ON-S RGCs,
909 cells were filled with sulphorhodamine 101. ON-T RGC dendrites were then recorded at the
910 same location but deeper into the retina (Krieger et al., 2017).
911
912 *Visual stimulation*
913
914 Visual stimuli were presented from a photopic mean background illumination (~3,300 rhodopsin
915 isomerizations per rod per second (R*/rod/s)) to focus specifically on cone-mediated signaling
916 (Grimes et al., 2018). Visual stimuli for electrophysiological recordings were generated using
917 Stage Visual Stimulation Software (http://stage-vss.github.io). For all electrophysiological
918 recordings except those in Figs. 6C-F and S8, light stimuli consisted of a spatially uniform
919 circular spot (520 μm diameter) delivered from a LED (405 nm peak output; Hosfelt) that was
920 focused through the microscope substage condenser (Kuo et al., 2016). In the experiments
921 shown in Figs. 6C-F and S8, a Digital Light Processing (DLP) projector driven by a 405 nm LED
922 (Wintech Digital) was used to project spots of various sizes through the microscope objective
923 (Kuo et al., 2020). For iGluSnFR imaging (Fig. 5), background illuminance was kept around
924 1000 photons/μm^2/s. For experiments, static spots of different sizes were generated and
925 presented using StimGen software (https://github.com/benmurphybaum/StimGen). Stimuli were
926 presented via a DLP through the substage condenser focused onto the photoreceptor layer of
927 the retina. All visual stimuli were presented 4 s after the start of the recording for a duration of 2
928 s.
929
930 *Data analysis and statistics*
931
932 Spike triggered average (STA) waveforms (Fig. 1) and linear-nonlinear (LN) models of light-
933 driven RGC (Fig. 2) and bipolar cell (Fig.4) responses were derived from responses to randomly
934 fluctuating light stimuli (Gaussian distribution of light intensities with standard deviation = 50% of
935 mean intensity; 0-60 Hz bandwidth) as described previously (Chichilnisky, 2001; Kim and Rieke,
936 2001; Rieke, 2001). For LN model construction, the linear filter was calculated by computing the
937 cross-correlation of the light stimulus with the measured voltage (bipolar cell) or current (RGC)
938 response and dividing the result by the power spectrum of the stimulus. The static nonlinearity
939 was constructed from a point-by-point comparison of the predicted filter output with the
940 measured response and binning the result along the prediction axis. In almost all cases, the
941 linear filter had a biphasic shape with initial and secondary lobes that are opposite polarity. A
942 small number of bipolar cells had triphasic filters (Fig. S7). We quantified the kinetics of each
943 STA or linear filter by measuring the time at which the STA/filter waveform crossed zero ("zero-
944 cross time"; e.g. Fig. 1C, left) between the first and second lobes of the filter (e.g. between peak
945 and trough of STA waveforms) and by calculating a biphasic index = |A| / |B|, where |B| is the
946 absolute peak amplitude of the initial lobe of the filter and |A| is the amplitude of the peak
947 amplitude of the secondary lobe (e.g. Fig. 2C, right). We quantified the kinetics of responses to
948 light step stimuli by calculating the time between light step onset and the peak amplitude

949 response (“time to peak”; e.g. Fig. 2E, left) and dividing the mean steady-state response
950 (calculated from the last 100 ms light step increment) by the peak amplitude initial response at
951 step onset (and multiplying by 100) (e.g. Fig. 2E, right). We note that alternative measures of
952 step response or linear filter kinetics than those presented in Fig. 4 were also not statistically
953 different between bipolar cell subtypes (not shown). For light step-evoked responses, steady-
954 state measurements were obtained from the mean current/voltage over the last 100 ms of the
955 500 ms light steps (electrophysiology) or the mean fluorescence over the last 1 sec of the 2 sec
956 light step (iGluSnFR). Statistical tests were performed using MATLAB (Mathworks) or Igor Pro
957 (WaveMetrics) software.
958
959 *Biolistic transfection*
960
961 DNA plasmids encoding mTFP1-myc (24 µg) and PSD95-mCherry (12 µg) under the control of
962 the cytomegalovirus (CMV) promoter were coated onto gold particles (1.6 µm diameter, 12.5
963 mg, Bio-Rad). Using a Helios gene gun (40 psi, Bio-Rad), these particles were then delivered to
964 retinal ganglion cells in whole-mount retinas. Subsequently, the transfected retinas were
965 incubated overnight in mACSF within a humid, oxygenated chamber maintained at 33°C.
966 *Immunohistochemistry*
967
968 Retinal sections (60 µm thick) were prepared using a vibratome (Leica) from retinal whole
969 mount retinas of *Gjd2-EGFP* mice. Both whole mount retinas and retinal sections were fixed in
970 4% PFA for 30 minutes. Retinal sections were embedded in low melting point agarose (Sigma-
971 Aldrich). Retinal tissues were first incubated with blocking solution (5% normal donkey serum,
972 0.5% Triton-X100 in PBS, Sigma-Aldrich) for 2 hours at 4°C, then incubated overnight at 4°C
973 with primary antibodies dissolved in blocking solution. Excess primary antibody was rinsed 3x10
974 minutes with PBS, then sections were incubated for 2 hours with secondary antibodies
975 dissolved in PBS. Excess secondary antibody was rinsed 3x10 minutes with PBS and sections
976 were mounted on standard microscopy glass slides using Vectashield mounting medium
977 (Vector). Primary antibody used in the study were: goat anti-ChAT diluted 1:1000 Chemicon
978 AB144P, mouse anti-CaBP5 diluted 1:1000 courtesy of Dr. Haeseleer, mouse anti-myc diluted
979 at 1:1000, chicken anti-GFP diluted at 1:1000. Secondary antibody were donkey anti-goat IgG
980 Dylight-568 diluted 1:1000, donkey anti-mouse Dylight-647 diluted 1:1000, donkey anti-mouse
981 Dylight-405 diluted at 1:1000 , donkey anti-chicken Alexa 488, the nuclear dye TOPRO3 (diluted
982 1:200, Thermo-Fisher).
983
984 *Near-infrared branding (NIRB) and serial block face scanning electron microscopy (SBFSEM)*
985
986 Two neighboring ON-T RGCs were physiologically identified in *Gjd2-EGFP* mice. After
987 identifying ON-T RGCs via their characteristic step-evoked extracellular spike response (e.g.
988 Figure 1B), they were filled with Alexa 488 or Alexa 555. Dendritic arbors and T5i-BC axonal
989 arbors were imaged using a confocal microscope. The retina was then fixed with 4%
990 glutaraldehyde for 30 minutes at room temperature (RT). The retina was washed with 0.1M Na+
991 Cacodylate buffer for three times and flat-mounted with 0.1M Na+ Cacodylate buffer. To
992 relocate the two RGCs under electron microscopy, we applied the near-infrared branding
993 (NIRB) technique previously published to burn fiducial markers in the retina (Bishop et al.). After
994 NIRBing, the retina tissue was unmounted and fixed in 4% glutaraldehyde overnight. The retina
995 was processed for SBFSEM subsequently according to the protocol described previously (Della
996 Santina et al., 2016). Briefly, the tissue was initially treated with reduced osmium for 1 hour in
997 the refrigerator. Subsequently, after washing with double-distilled H2O (ddH2O), the tissue was
998 placed in a freshly prepared thiocarbohydrazide solution for 20 minutes at RT. Following
999 another round of ddH2O rinsing, the tissue was incubated in 2% osmium tetroxide for 30

1000 minutes at RT. After rinsing, the sample was incubated in 1% uranyl acetate at 4°C overnight.
1001 Post-wash, the tissue was stained with Walton's lead aspartate for 30 minutes at 60°C.
1002 Following another wash, the retinal piece underwent dehydration using a graded alcohol series
1003 (20%, 50%, 70%, 90%, 100%, 100%), each step lasting 5 minutes, followed by two changes of
1004 100% propylene oxide at RT for 10 minutes each. Finally, the tissue was embedded in Epon.
1005 The resulting block was then trimmed and mounted in the SBEM microscope (GATAN/Zeiss
1006 SIGMA, 3View), and image stacks were acquired at a voxel size of 5 x 5 x 50 nm.
1007
1008
1009

1010 ***References***
1011

1012 Angueyra JM, Rieke F. 2013. Origin and effect of phototransduction noise in primate cone
1013 photoreceptors. *Nat Neurosci* **16**:1692–1700. doi:10.1038/nn.3534
1014 Asari H, Meister M. 2014. The projective field of retinal bipolar cells and its modulation by
1015 visual context. *Neuron* **81**:641–652. doi:10.1016/j.neuron.2013.11.029
1016 Asari H, Meister M. 2012. Divergence of visual channels in the inner retina. *Nat Neurosci*
1017 **15**:1581–1589. doi:10.1038/nn.3241
1018 Awatramani GB, Slaughter MM. 2000. Origin of transient and sustained responses in ganglion
1019 cells of the retina. *J Neurosci* **20**:7087–7095. doi:10.1523/JNEUROSCI.20-18-07087.2000
1020 Babai N, Sendelbeck A, Regus-Leidig H, Fuchs M, Mertins J, Reim K, Brose N, Feigenspan A,
1021 Brandstätter JH. 2016. Functional Roles of Complexin 3 and Complexin 4 at Mouse
1022 Photoreceptor Ribbon Synapses. *J Neurosci* **36**:6651–6667.
1023 doi:10.1523/JNEUROSCI.4335-15.2016
1024 Baden T, Berens P, Bethge M, Euler T. 2013. Spikes in mammalian bipolar cells support
1025 temporal layering of the inner retina. *Curr Biol* **23**:48–52. doi:10.1016/j.cub.2012.11.006
1026 Baden T, Berens P, Franke K, Román Rosón M, Bethge M, Euler T. 2016. The functional diversity
1027 of retinal ganglion cells in the mouse. *Nature* **529**:345–350. doi:10.1038/nature16468
1028 Bae JA, Mu S, Kim JS, Turner NL, Tartavull I, Kemnitz N, Jordan CS, Norton AD, Silversmith WM,
1029 Prentki R, Sorek M, David C, Jones DL, Bland D, Sterling ALR, Park J, Briggman KL, Seung
1030 HS, Eyewirers. 2018. Digital Museum of Retinal Ganglion Cells with Dense Anatomy and
1031 Physiology. *Cell* **173**:1293-1306.e19. doi:10.1016/j.cell.2018.04.040
1032 Beaudoin DL, Kupershtok M, Demb JB. 2019. Selective synaptic connections in the retinal
1033 pathway for night vision. *J Comp Neurol* **527**:117–132. doi:10.1002/cne.24313
1034 Bishop D, Nikić I, Brinkoetter M, Knecht S, Potz S, Kerschensteiner M, Misgeld T. 2011. Near-
1035 infrared branding efficiently correlates light and electron microscopy. *Nat Methods*
1036 **8**:568–570. doi:10.1038/nmeth.1622
1037 Borghuis BG, Marvin JS, Looger LL, Demb JB. 2013a. Two-photon imaging of nonlinear
1038 glutamate release dynamics at bipolar cell synapses in the mouse retina. *J Neurosci*
1039 **33**:10972–10985. doi:10.1523/JNEUROSCI.1241-13.2013
1040 Borghuis BG, Marvin JS, Looger LL, Demb JB. 2013b. Two-photon imaging of nonlinear
1041 glutamate release dynamics at bipolar cell synapses in the mouse retina. *J Neurosci*
1042 **33**:10972–10985. doi:10.1523/JNEUROSCI.1241-13.2013
1043 Brombas A, Zhou X, Williams SR. 2022. Light-evoked dendritic spikes in sustained but not
1044 transient rabbit retinal ganglion cells. *Neuron* **110**:2802-2814.e3.
1045 doi:10.1016/j.neuron.2022.06.009
1046 Burrone J, Lagnado L. 2000. Synaptic depression and the kinetics of exocytosis in retinal bipolar
1047 cells. *J Neurosci* **20**:568–578. doi:10.1523/JNEUROSCI.20-02-00568.2000
1048 Burrone J, Neves G, Gomis A, Cooke A, Lagnado L. 2002. Endogenous calcium buffers regulate
1049 fast exocytosis in the synaptic terminal of retinal bipolar cells. *Neuron* **33**:101–112.
1050 doi:10.1016/s0896-6273(01)00565-7
1051 Cafaro J, Rieke F. 2013. Regulation of spatial selectivity by crossover inhibition. *J Neurosci*
1052 **33**:6310–6320. doi:10.1523/JNEUROSCI.4964-12.2013

1053 Cangiano L, Asteriti S, Cervetto L, Gargini C. 2012. The photovoltage of rods and cones in the
1054 dark-adapted mouse retina. *J Physiol* **590**:3841–3855. doi:10.1113/jphysiol.2011.226878
1055 Chang L, Ran Y, Yang M, Auferkorte O, Butz E, Hüser L, Haverkamp S, Euler T, Schubert T. 2023.
1056 Spike desensitisation as a mechanism for high-contrast selectivity in retinal ganglion
1057 cells. *Front Cell Neurosci* **17**:1337768. doi:10.3389/fncel.2023.1337768
1058 Chichilnisky EJ. 2001. A simple white noise analysis of neuronal light responses. *Network*
1059 **12**:199–213.
1060 Cleland BG, Levick WR, Sanderson KJ. 1973. Properties of sustained and transient ganglion cells
1061 in the cat retina. *J Physiol* **228**:649–680. doi:10.1113/jphysiol.1973.sp010105
1062 Cohen E, Sterling P. 1990. Demonstration of cell types among cone bipolar neurons of cat
1063 retina. *Philos Trans R Soc Lond B Biol Sci* **330**:305–321. doi:10.1098/rstb.1990.0201
1064 Demb JB, Singer JH. 2012. Intrinsic properties and functional circuitry of the AII amacrine cell.
1065 *Vis Neurosci* **29**:51–60. doi:10.1017/S0952523811000368
1066 Dembla E, Dembla M, Maxeiner S, Schmitz F. 2020. Synaptic ribbons foster active zone stability
1067 and illumination-dependent active zone enrichment of RIM2 and Cav1.4 in
1068 photoreceptor synapses. *Sci Rep* **10**:5957. doi:10.1038/s41598-020-62734-0
1069 DeVries SH. 2000. Bipolar cells use kainate and AMPA receptors to filter visual information into
1070 separate channels. *Neuron* **28**:847–856. doi:10.1016/s0896-6273(00)00158-6
1071 Diamond JS. 2017. Inhibitory Interneurons in the Retina: Types, Circuitry, and Function. *Annu*
1072 *Rev Vis Sci* **3**:1–24. doi:10.1146/annurev-vision-102016-061345
1073 Ding H, Smith RG, Poleg-Polsky A, Diamond JS, Briggman KL. 2016. Species-specific wiring for
1074 direction selectivity in the mammalian retina. *Nature* **535**:105–110.
1075 doi:10.1038/nature18609
1076 Dowling JE, Boycott BB. 1966. Organization of the primate retina: electron microscopy. *Proc R*
1077 *Soc Lond B Biol Sci* **166**:80–111. doi:10.1098/rspb.1966.0086
1078 Duan X, Krishnaswamy A, De la Huerta I, Sanes JR. 2014. Type II cadherins guide assembly of a
1079 direction-selective retinal circuit. *Cell* **158**:793–807. doi:10.1016/j.cell.2014.06.047
1080 Euler T, Haverkamp S, Schubert T, Baden T. 2014. Retinal bipolar cells: elementary building
1081 blocks of vision. *Nat Rev Neurosci* **15**:507–519. doi:10.1038/nrn3783
1082 Euler T, Masland RH. 2000. Light-evoked responses of bipolar cells in a mammalian retina. *J*
1083 *Neurophysiol* **83**:1817–1829. doi:10.1152/jn.2000.83.4.1817
1084 Farrow K, Teixeira M, Szikra T, Viney TJ, Balint K, Yonehara K, Roska B. 2013. Ambient
1085 illumination toggles a neuronal circuit switch in the retina and visual perception at cone
1086 threshold. *Neuron* **78**:325–338. doi:10.1016/j.neuron.2013.02.014
1087 Franke K, Berens P, Schubert T, Bethge M, Euler T, Baden T. 2017. Inhibition decorrelates visual
1088 feature representations in the inner retina. *Nature* **542**:439–444.
1089 doi:10.1038/nature21394
1090 Ghosh KK, Bujan S, Haverkamp S, Feigenspan A, Wässle H. 2004. Types of bipolar cells in the
1091 mouse retina. *J Comp Neurol* **469**:70–82. doi:10.1002/cne.10985
1092 Goetz J, Jessen ZF, Jacobi A, Mani A, Cooler S, Greer D, Kadri S, Segal J, Shekhar K, Sanes JR,
1093 Schwartz GW. 2022. Unified classification of mouse retinal ganglion cells using function,
1094 morphology, and gene expression. *Cell Rep* **40**:111040.
1095 doi:10.1016/j.celrep.2022.111040

1096 Gollisch T, Meister M. 2010. Eye smarter than scientists believed: neural computations in
1097 circuits of the retina. *Neuron* **65**:150–164. doi:10.1016/j.neuron.2009.12.009
1098 Grabner CP, Futagi D, Shi J, Bindokas V, Kitano K, Schwartz EA, DeVries SH. 2023. Mechanisms
1099 of simultaneous linear and nonlinear computations at the mammalian cone
1100 photoreceptor synapse. *Nat Commun* **14**:3486. doi:10.1038/s41467-023-38943-2
1101 Grabner CP, Moser T. 2021. The mammalian rod synaptic ribbon is essential for Cav channel
1102 facilitation and ultrafast synaptic vesicle fusion. *Elife* **10**:e63844.
1103 doi:10.7554/eLife.63844
1104 Grabner CP, Ratliff CP, Light AC, DeVries SH. 2016. Mechanism of High-Frequency Signaling at a
1105 Depressing Ribbon Synapse. *Neuron* **91**:133–145. doi:10.1016/j.neuron.2016.05.019
1106 Greene MJ, Kim JS, Seung HS, EyeWirers. 2016. Analogous Convergence of Sustained and
1107 Transient Inputs in Parallel On and Off Pathways for Retinal Motion Computation. *Cell*
1108 *Rep* **14**:1892–1900. doi:10.1016/j.celrep.2016.02.001
1109 Grimes WN, Baudin J, Azevedo AW, Rieke F. 2018. Range, routing and kinetics of rod signaling in
1110 primate retina. *Elife* **7**:e38281. doi:10.7554/eLife.38281
1111 Grimes WN, Schwartz GW, Rieke F. 2014. The synaptic and circuit mechanisms underlying a
1112 change in spatial encoding in the retina. *Neuron* **82**:460–473.
1113 doi:10.1016/j.neuron.2014.02.037
1114 Hellmer CB, Zhou Y, Fyk-Kolodziej B, Hu Z, Ichinose T. 2016. Morphological and physiological
1115 analysis of type-5 and other bipolar cells in the Mouse Retina. *Neuroscience* **315**:246–
1116 258. doi:10.1016/j.neuroscience.2015.12.016
1117 Helmstaedter M, Briggman KL, Turaga SC, Jain V, Seung HS, Denk W. 2013. Connectomic
1118 reconstruction of the inner plexiform layer in the mouse retina. *Nature* **500**:168–174.
1119 doi:10.1038/nature12346
1120 Hsiang J-C, Shen N, Soto F, Kerschensteiner D. 2024. Distributed feature representations of
1121 natural stimuli across parallel retinal pathways. *Nat Commun* **15**:1920.
1122 doi:10.1038/s41467-024-46348-y
1123 Huang L, Max M, Margolskee RF, Su H, Masland RH, Euler T. 2003. G protein subunit G gamma
1124 13 is coexpressed with G alpha o, G beta 3, and G beta 4 in retinal ON bipolar cells. *J*
1125 *Comp Neurol* **455**:1–10. doi:10.1002/cne.10396
1126 Huang L, Shanker YG, Dubauskaite J, Zheng JZ, Yan W, Rosenzweig S, Spielman AI, Max M,
1127 Margolskee RF. 1999. Ggamma13 colocalizes with gustducin in taste receptor cells and
1128 mediates IP3 responses to bitter denatonium. *Nat Neurosci* **2**:1055–1062.
1129 doi:10.1038/15981
1130 Hull C, Studholme K, Yazulla S, von Gersdorff H. 2006. Diurnal changes in exocytosis and the
1131 number of synaptic ribbons at active zones of an ON-type bipolar cell terminal. *J*
1132 *Neurophysiol* **96**:2025–2033. doi:10.1152/jn.00364.2006
1133 Ichinose T, Fyk-Kolodziej B, Cohn J. 2014. Roles of ON cone bipolar cell subtypes in temporal
1134 coding in the mouse retina. *J Neurosci* **34**:8761–8771. doi:10.1523/JNEUROSCI.3965-
1135 13.2014
1136 Ichinose T, Hellmer CB. 2016. Differential signalling and glutamate receptor compositions in the
1137 OFF bipolar cell types in the mouse retina. *J Physiol* **594**:883–894. doi:10.1113/JP271458

1138 Ikeda H, Wright MJ. 1972. Receptive field organization of “sustained” and “transient” retinal
1139 ganglion cells which subserve different function roles. *J Physiol* **227**:769–800.
1140 doi:10.1113/jphysiol.1972.sp010058
1141 Jackman SL, Choi S-Y, Thoreson WB, Rabl K, Bartoletti TM, Kramer RH. 2009. Role of the
1142 synaptic ribbon in transmitting the cone light response. *Nat Neurosci* **12**:303–310.
1143 doi:10.1038/nn.2267
1144 Jadzinsky PD, Baccus SA. 2013. Transformation of visual signals by inhibitory interneurons in
1145 retinal circuits. *Annu Rev Neurosci* **36**:403–428. doi:10.1146/annurev-neuro-062012-
1146 170315
1147 Jarsky T, Cembrowski M, Logan SM, Kath WL, Riecke H, Demb JB, Singer JH. 2011. A Synaptic
1148 Mechanism for Retinal Adaptation to Luminance and Contrast. *J Neurosci* **31**:11003–
1149 11015. doi:10.1523/JNEUROSCI.2631-11.2011
1150 Ke J-B, Wang YV, Borghuis BG, Cembrowski MS, Riecke H, Kath WL, Demb JB, Singer JH. 2014.
1151 Adaptation to background light enables contrast coding at rod bipolar cell synapses.
1152 *Neuron* **81**:388–401. doi:10.1016/j.neuron.2013.10.054
1153 Kerschensteiner D. 2022. Feature Detection by Retinal Ganglion Cells. *Annu Rev Vis Sci* **8**:135–
1154 169. doi:10.1146/annurev-vision-100419-112009
1155 Kim KJ, Rieke F. 2001. Temporal contrast adaptation in the input and output signals of
1156 salamander retinal ganglion cells. *J Neurosci* **21**:287–299. doi:10.1523/JNEUROSCI.21-
1157 01-00287.2001
1158 Krieger B, Qiao M, Rousso DL, Sanes JR, Meister M. 2017. Four alpha ganglion cell types in
1159 mouse retina: Function, structure, and molecular signatures. *PLoS One* **12**:e0180091.
1160 doi:10.1371/journal.pone.0180091
1161 Kuo SP, Chiang P-P, Nippert AR, Newman EA. 2020. Spatial Organization and Dynamics of the
1162 Extracellular Space in the Mouse Retina. *J Neurosci* **40**:7785–7794.
1163 doi:10.1523/JNEUROSCI.1717-20.2020
1164 Kuo SP, Schwartz GW, Rieke F. 2016. Nonlinear Spatiotemporal Integration by Electrical and
1165 Chemical Synapses in the Retina. *Neuron* **90**:320–332.
1166 doi:10.1016/j.neuron.2016.03.012
1167 Lagnado L, Schmitz F. 2015. Ribbon Synapses and Visual Processing in the Retina. *Annu Rev Vis*
1168 *Sci* **1**:235–262. doi:10.1146/annurev-vision-082114-035709
1169 Marc RE, Anderson JR, Jones BW, Sigulinsky CL, Lauritzen JS. 2014. The AII amacrine cell
1170 connectome: a dense network hub. *Front Neural Circuits* **8**:104.
1171 doi:10.3389/fncir.2014.00104
1172 Margolis DJ, Gartland AJ, Euler T, Detwiler PB. 2010. Dendritic Calcium Signaling in ON and OFF
1173 Mouse Retinal Ganglion Cells. *J Neurosci* **30**:7127–7138. doi:10.1523/JNEUROSCI.5694-
1174 09.2010
1175 Masland RH. 2012. The Neuronal Organization of the Retina. *Neuron* **76**:266–280.
1176 doi:10.1016/j.neuron.2012.10.002
1177 Maxeiner S, Luo F, Tan A, Schmitz F, Südhof TC. 2016. How to make a synaptic ribbon: RIBEYE
1178 deletion abolishes ribbons in retinal synapses and disrupts neurotransmitter release.
1179 *EMBO J* **35**:1098–1114. doi:10.15252/embj.201592701
1180 McGuire BA, Stevens JK, Sterling P. 1984. Microcircuitry of bipolar cells in cat retina. *J Neurosci*
1181 **4**:2920–2938. doi:10.1523/JNEUROSCI.04-12-02920.1984

1182 Mehta B, Snellman J, Chen S, Li W, Zenisek D. 2013. Synaptic ribbons influence the size and
1183 frequency of miniature-like evoked postsynaptic currents. *Neuron* **77**:516–527.
1184 doi:10.1016/j.neuron.2012.11.024
1185 Morgan JL, Soto F, Wong ROL, Kerschensteiner D. 2011. Development of cell type-specific
1186 connectivity patterns of converging excitatory axons in the retina. *Neuron* **71**:1014–
1187 1021. doi:10.1016/j.neuron.2011.08.025
1188 Neves G, Lagnado L. 1999. The kinetics of exocytosis and endocytosis in the synaptic terminal of
1189 goldfish retinal bipolar cells. *J Physiol* **515 (Pt 1)**:181–202. doi:10.1111/j.1469-
1190 7793.1999.181ad.x
1191 Nikolaev A, Leung K-M, Odermatt B, Lagnado L. 2013. Synaptic mechanisms of adaptation and
1192 sensitization in the retina. *Nat Neurosci* **16**:934–941. doi:10.1038/nn.3408
1193 Nirenberg S, Meister M. 1997. The light response of retinal ganglion cells is truncated by a
1194 displaced amacrine circuit. *Neuron* **18**:637–650. doi:10.1016/s0896-6273(00)80304-9
1195 Oesch NW, Diamond JS. 2011. Ribbon synapses compute temporal contrast and encode
1196 luminance in retinal rod bipolar cells. *Nat Neurosci* **14**:1555–1561. doi:10.1038/nn.2945
1197 Okawa H, Yu W-Q, Matti U, Schwarz K, Odermatt B, Zhong H, Tsukamoto Y, Lagnado L, Rieke F,
1198 Schmitz F, Wong ROL. 2019. Dynamic assembly of ribbon synapses and circuit
1199 maintenance in a vertebrate sensory system. *Nat Commun* **10**:2167.
1200 doi:10.1038/s41467-019-10123-1
1201 Pangrsic T, Singer JH, Koschak A. 2018. Voltage-Gated Calcium Channels: Key Players in Sensory
1202 Coding in the Retina and the Inner Ear. *Physiol Rev* **98**:2063–2096.
1203 doi:10.1152/physrev.00030.2017
1204 Pottackal J, Singer JH, Demb JB. 2021. Computational and Molecular Properties of Starburst
1205 Amacrine Cell Synapses Differ With Postsynaptic Cell Type. *Front Cell Neurosci*
1206 **15**:660773. doi:10.3389/fncel.2021.660773
1207 Puthussery T, Venkataramani S, Gayet-Primo J, Smith RG, Taylor WR. 2013. NaV1.1 channels in
1208 axon initial segments of bipolar cells augment input to magnocellular visual pathways in
1209 the primate retina. *J Neurosci* **33**:16045–16059. doi:10.1523/JNEUROSCI.1249-13.2013
1210 Rabl K, Cadetti L, Thoreson WB. 2006. Paired-pulse depression at photoreceptor synapses. *J*
1211 *Neurosci* **26**:2555–2563. doi:10.1523/JNEUROSCI.3667-05.2006
1212 Ran Y, Huang Z, Baden T, Schubert T, Baayen H, Berens P, Franke K, Euler T. 2020. Type-specific
1213 dendritic integration in mouse retinal ganglion cells. *Nat Commun* **11**:2101.
1214 doi:10.1038/s41467-020-15867-9
1215 Rieke F. 2001. Temporal contrast adaptation in salamander bipolar cells. *J Neurosci* **21**:9445–
1216 9454.
1217 Rodieck RW. 1991. The density recovery profile: a method for the analysis of points in the plane
1218 applicable to retinal studies. *Vis Neurosci* **6**:95–111. doi:10.1017/s095252380001049x
1219 Roska B, Werblin F. 2001. Vertical interactions across ten parallel, stacked representations in
1220 the mammalian retina. *Nature* **410**:583–587. doi:10.1038/35069068
1221 Sabbah S, Papendorp C, Koplas E, Beltoja M, Etebari C, Gunesch AN, Carrete L, Kim MT, Manoff
1222 G, Bhatia-Lin A, Zhao T, Schreck D, Dowling H, Briggman KL, Berson DM. 2018. Synaptic
1223 circuits for irradiance coding by intrinsically photosensitive retinal ganglion cells
1224 (preprint). Neuroscience. doi:10.1101/442954

1225 Sagdullaev BT, McCall MA, Lukasiewicz PD. 2006. Presynaptic inhibition modulates spillover,
1226 creating distinct dynamic response ranges of sensory output. *Neuron* **50**:923–935.
1227 doi:10.1016/j.neuron.2006.05.015
1228 Saszik S, DeVries SH. 2012. A mammalian retinal bipolar cell uses both graded changes in
1229 membrane voltage and all-or-nothing Na+ spikes to encode light. *J Neurosci* **32**:297–307.
1230 doi:10.1523/JNEUROSCI.2739-08.2012
1231 Schwartz GW, Okawa H, Dunn FA, Morgan JL, Kerschensteiner D, Wong RO, Rieke F. 2012. The
1232 spatial structure of a nonlinear receptive field. *Nat Neurosci* **15**:1572–1580.
1233 doi:10.1038/nn.3225
1234 Shekhar K, Lapan SW, Whitney IE, Tran NM, Macosko EZ, Kowalczyk M, Adiconis X, Levin JZ,
1235 Nemesh J, Goldman M, McCarroll SA, Cepko CL, Regev A, Sanes JR. 2016.
1236 Comprehensive Classification of Retinal Bipolar Neurons by Single-Cell Transcriptomics.
1237 *Cell* **166**:1308-1323.e30. doi:10.1016/j.cell.2016.07.054
1238 Sigulinsky CL, Anderson JR, Kerzner E, Rapp CN, Pfeiffer RL, Rodman TM, Emrich DP, Rapp KD,
1239 Nelson NT, Lauritzen JS, Meyer M, Marc RE, Jones BW. 2020. Network Architecture of
1240 Gap Junctional Coupling among Parallel Processing Channels in the Mammalian Retina. *J*
1241 *Neurosci* **40**:4483–4511. doi:10.1523/JNEUROSCI.1810-19.2020
1242 Singer JH, Diamond JS. 2006. Vesicle depletion and synaptic depression at a mammalian ribbon
1243 synapse. *J Neurophysiol* **95**:3191–3198. doi:10.1152/jn.01309.2005
1244 Singer JH, Diamond JS. 2003. Sustained Ca2+ entry elicits transient postsynaptic currents at a
1245 retinal ribbon synapse. *J Neurosci* **23**:10923–10933. doi:10.1523/JNEUROSCI.23-34-
1246 10923.2003
1247 Slaughter MM, Miller RF. 1981. 2-amino-4-phosphonobutyric acid: a new pharmacological tool
1248 for retina research. *Science* **211**:182–185. doi:10.1126/science.6255566
1249 Snellman J, Mehta B, Babai N, Bartoletti TM, Akmentin W, Francis A, Matthews G, Thoreson W,
1250 Zenisek D. 2011. Acute destruction of the synaptic ribbon reveals a role for the ribbon in
1251 vesicle priming. *Nat Neurosci* **14**:1135–1141. doi:10.1038/nn.2870
1252 Snellman J, Zenisek D, Nawy S. 2009. Switching between transient and sustained signalling at
1253 the rod bipolar-AII amacrine cell synapse of the mouse retina. *J Physiol* **587**:2443–2455.
1254 doi:10.1113/jphysiol.2008.165241
1255 Srivastava P, de Rosenroll G, Matsumoto A, Michaels T, Turple Z, Jain V, Sethuramanujam S,
1256 Murphy-Baum BL, Yonehara K, Awatramani GB. 2022. Spatiotemporal properties of
1257 glutamate input support direction selectivity in the dendrites of retinal starburst
1258 amacrine cells. *Elife* **11**:e81533. doi:10.7554/eLife.81533
1259 Swygart D, Yu W-Q, Takeuchi S, Wong ROL, Schwartz GW. 2024. A presynaptic source drives
1260 differing levels of surround suppression in two mouse retinal ganglion cell types. *Nat*
1261 *Commun* **15**:599. doi:10.1038/s41467-024-44851-w
1262 Szikra T, Trenholm S, Drinnenberg A, Jüttner J, Raics Z, Farrow K, Biel M, Awatramani G, Clark
1263 DA, Sahel J-A, da Silveira RA, Roska B. 2014. Rods in daylight act as relay cells for cone-
1264 driven horizontal cell-mediated surround inhibition. *Nat Neurosci* **17**:1728–1735.
1265 doi:10.1038/nn.3852
1266 Taylor WR, Vaney DI. 2002. Diverse synaptic mechanisms generate direction selectivity in the
1267 rabbit retina. *J Neurosci* **22**:7712–7720.

1268 Tsukamoto Y, Omi N. 2017. Classification of Mouse Retinal Bipolar Cells: Type-Specific
1269 Connectivity with Special Reference to Rod-Driven AII Amacrine Pathways. *Front*
1270 *Neuroanat* **11**:92. doi:10.3389/fnana.2017.00092
1271 Vaney DI, Sivyer B, Taylor WR. 2012. Direction selectivity in the retina: symmetry and
1272 asymmetry in structure and function. *Nat Rev Neurosci* **13**:194–208.
1273 doi:10.1038/nrn3165
1274 Veruki ML, Hartveit E. 2002a. Electrical synapses mediate signal transmission in the rod
1275 pathway of the mammalian retina. *J Neurosci* **22**:10558–10566.
1276 doi:10.1523/JNEUROSCI.22-24-10558.2002
1277 Veruki ML, Hartveit E. 2002b. AII (Rod) amacrine cells form a network of electrically coupled
1278 interneurons in the mammalian retina. *Neuron* **33**:935–946. doi:10.1016/s0896-
1279 6273(02)00609-8
1280 von Gersdorff H, Matthews G. 1997. Depletion and replenishment of vesicle pools at a ribbon-
1281 type synaptic terminal. *J Neurosci* **17**:1919–1927. doi:10.1523/JNEUROSCI.17-06-
1282 01919.1997
1283 von Gersdorff H, Vardi E, Matthews G, Sterling P. 1996. Evidence that vesicles on the synaptic
1284 ribbon of retinal bipolar neurons can be rapidly released. *Neuron* **16**:1221–1227.
1285 doi:10.1016/s0896-6273(00)80148-8
1286 Wakeham CM, Shi Q, Ren G, Haley TL, Duvoisin RM, von Gersdorff H, Morgans CW. 2023.
1287 Trophoblast glycoprotein is required for efficient synaptic vesicle exocytosis from retinal
1288 rod bipolar cells. *Front Cell Neurosci* **17**:1306006. doi:10.3389/fncel.2023.1306006
1289 Wan Q-F, Heidelberger R. 2011. Synaptic release at mammalian bipolar cell terminals. *Vis*
1290 *Neurosci* **28**:109–119. doi:10.1017/S0952523810000453
1291 Warwick RA, Kaushansky N, Sarid N, Golan A, Rivlin-Etzion M. 2018. Inhomogeneous Encoding
1292 of the Visual Field in the Mouse Retina. *Curr Biol* **28**:655-665.e3.
1293 doi:10.1016/j.cub.2018.01.016
1294 Wässle H, Puller C, Müller F, Haverkamp S. 2009. Cone contacts, mosaics, and territories of
1295 bipolar cells in the mouse retina. *J Neurosci* **29**:106–117. doi:10.1523/JNEUROSCI.4442-
1296 08.2009
1297 Werblin FS. 1970. Response of retinal cells to moving spots: intracellular recording in Necturus
1298 maculosus. *J Neurophysiol* **33**:342–350. doi:10.1152/jn.1970.33.3.342
1299 Werginz P, Raghuram V, Fried SI. 2020. Tailoring of the axon initial segment shapes the
1300 conversion of synaptic inputs into spiking output in OFF-α T retinal ganglion cells. *Sci*
1301 *Adv* **6**:eabb6642. doi:10.1126/sciadv.abb6642
1302 Wienbar S, Schwartz GW. 2022. Differences in spike generation instead of synaptic inputs
1303 determine the feature selectivity of two retinal cell types. *Neuron* **110**:2110-2123.e4.
1304 doi:10.1016/j.neuron.2022.04.012
1305 Wu SM, Gao F, Maple BR. 2000. Functional architecture of synapses in the inner retina:
1306 segregation of visual signals by stratification of bipolar cell axon terminals. *J Neurosci*
1307 **20**:4462–4470. doi:10.1523/JNEUROSCI.20-12-04462.2000
1308 Yu W-Q, Swanstrom R, Sigulinsky CL, Ahlquist RM, Knecht S, Jones BW, Berson DM, Wong RO.
1309 2023. Distinctive synaptic structural motifs link excitatory retinal interneurons to diverse
1310 postsynaptic partner types. *Cell Rep* **42**:112006. doi:10.1016/j.celrep.2023.112006

1311 Zhang Y, Kim I-J, Sanes JR, Meister M. 2012. The most numerous ganglion cell type of the
1312 mouse retina is a selective feature detector. *Proc Natl Acad Sci U S A* **109**:E2391-2398.
1313 doi:10.1073/pnas.1211547109
1314
1315

1316 ***Supplemental Information***
1317
1318

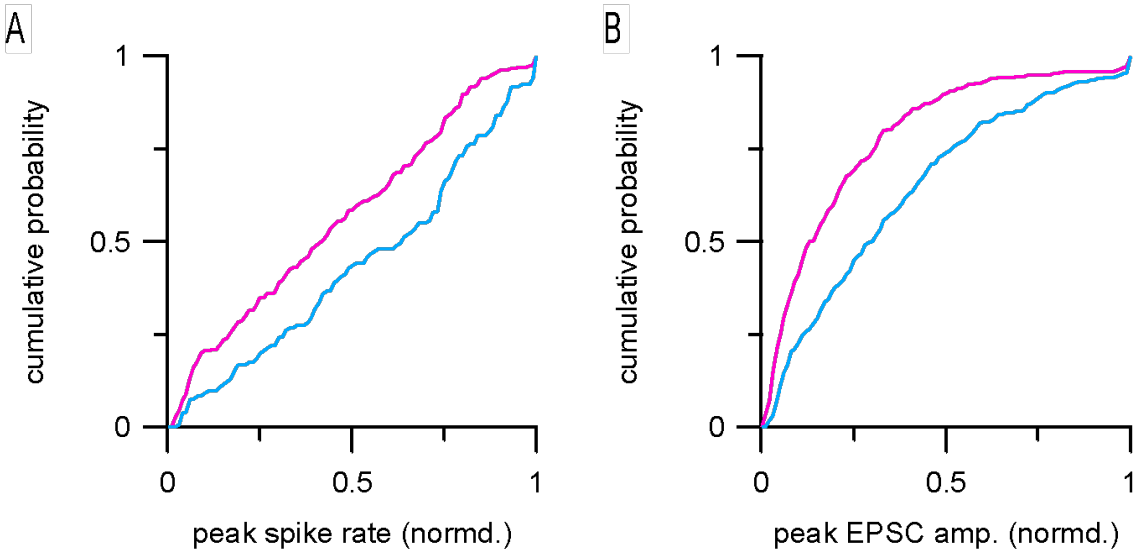

1319
1320
1321 ***Figure S1****. Noise-evoked responses are biased towards large amplitude events in ON-T*
1322 *compared to ON-S RGCs. (A) Spike event peak spike rate cumulative distributions for ON-T*
1323 *(cyan; n= 6 cells; 131 spike events) and ON-S RGC (magenta; n= 7 cells; 300 spike events).*
1324 *Firing rates from average responses to a repeated noise stimulus (see Fig. 1B-C) were*
1325 *normalized to the maximal firing rate in each cell before combining events across cells. (B)*
1326 *EPSC amplitude cumulative distributions for ON-T (n= 13 cells; 275 EPSCs) and ON-S (n= 10*
1327 *cells; 365 EPSCs) RGCs. Same stimulus and normalization procedure as in (A).*
1328

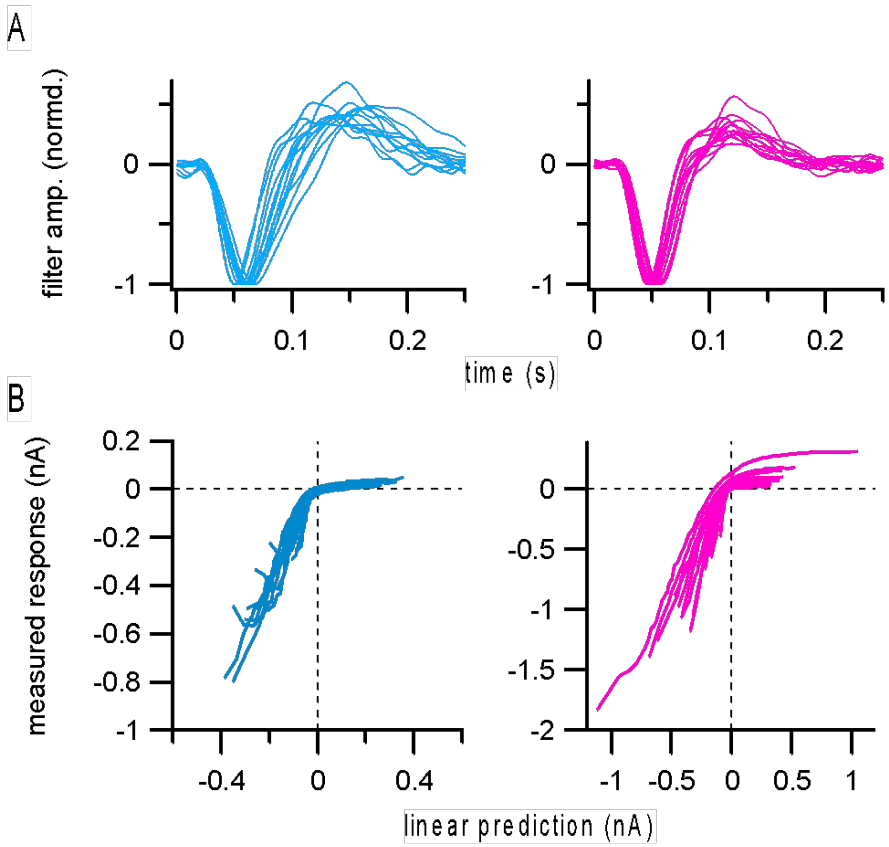

***Figure S2**. Linear-nonlinear models of excitatory synaptic input to ON-T and ON-S RGCs. (A) Linear filters computed from responses to non-repeated noise stimulus presentation. Lines show filters from individual ON-T (cyan; n= 13) and ON-S (magenta; n= 15) RGCs. Filters were normalized to the peak amplitude of the primary inward component to facilitate visual comparison of temporal responses. Same cells as shown in average filters in Fig. 2B. (B) Nonlinearities derived by plotting the predicted response (convolution of linear filter and stimulus) against the measured excitatory currents for each RGC shown in (A). Linear predictions were calculated using non-normalized filters.*

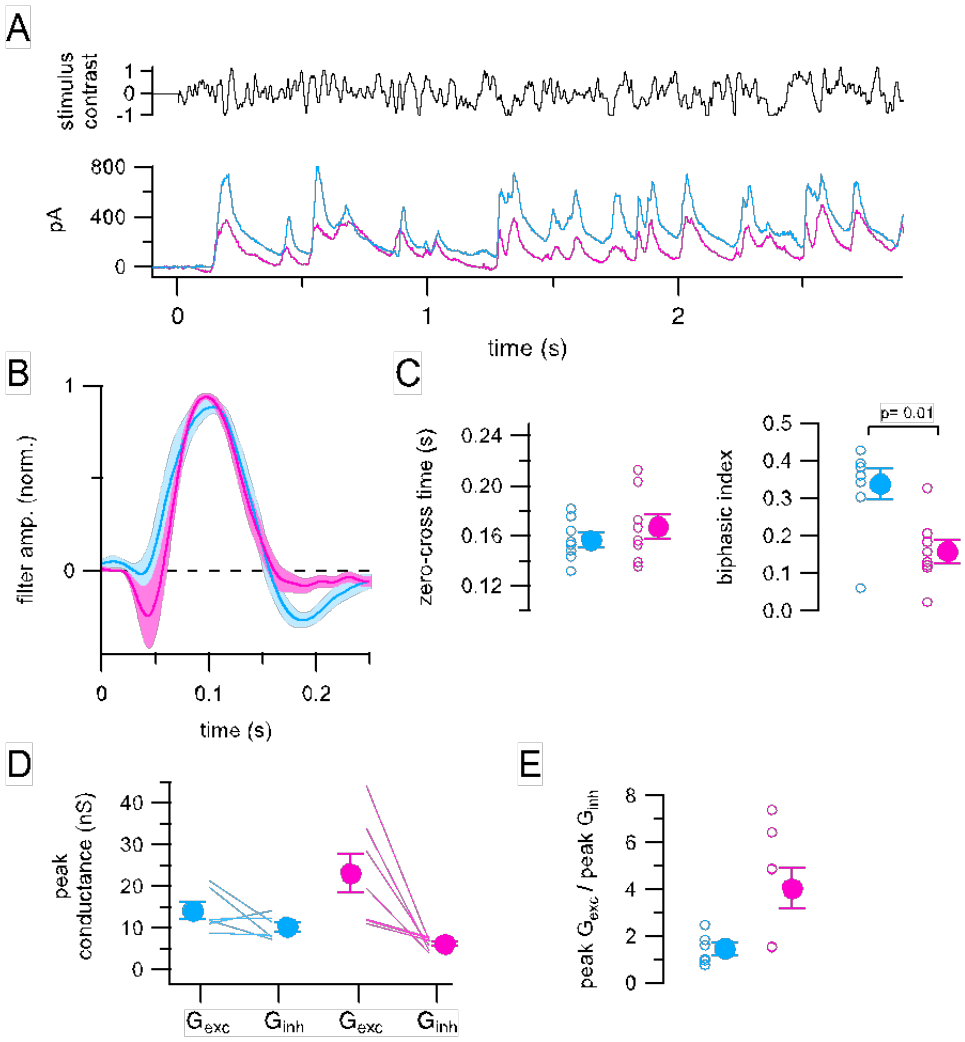

Figure S3. *Inhibitory synaptic input to ON-T and ON-S RGCs. (A) Inhibitory synaptic currents measured at V_{hold} = +10 mV (reversal potential for excitation) in example ON-T (cyan) and ON-S (pink) RGCs in response to same Gaussian noise stimulus as in Figs. 1-2. Traces show average currents from ten repetitions of the same stimulus and are baseline subtracted to facilitate comparison. (B) Linear filters computed from responses to non-repeated noise stimulus presentation. Lines and shaded areas show mean ± SEM of responses from ON-T (n= 8) and ON-S (n= 8) RGCs. (C) Quantification of filter kinetics in different RGCs. Zero-cross times were not significantly different (p= 0.57). Significance values from Wilcoxon rank sum test. (D) Peak amplitudes of excitatory and inhibitory conductances (G_{exc} and G_{inh}, respectively) calculated from average current responses to repeated noise stimuli such as shown in Figs. 2A and S3A. Lines connect peak G_{exc} and G_{inh} values measured from the same RGCs. Circles with error bars show mean ± SEM across ON-T RGCs (n= 6) and ON-S RGCs (n= 7) (E) Summary of peak excitatory/inhibitory conductance ratios. Open circles show measurements from individual cells and filled circles with error bars show mean ± SEM values. No significant difference between ON-T and ON-S RGCs; p= 0.10, Wilcoxon rank sum test.*

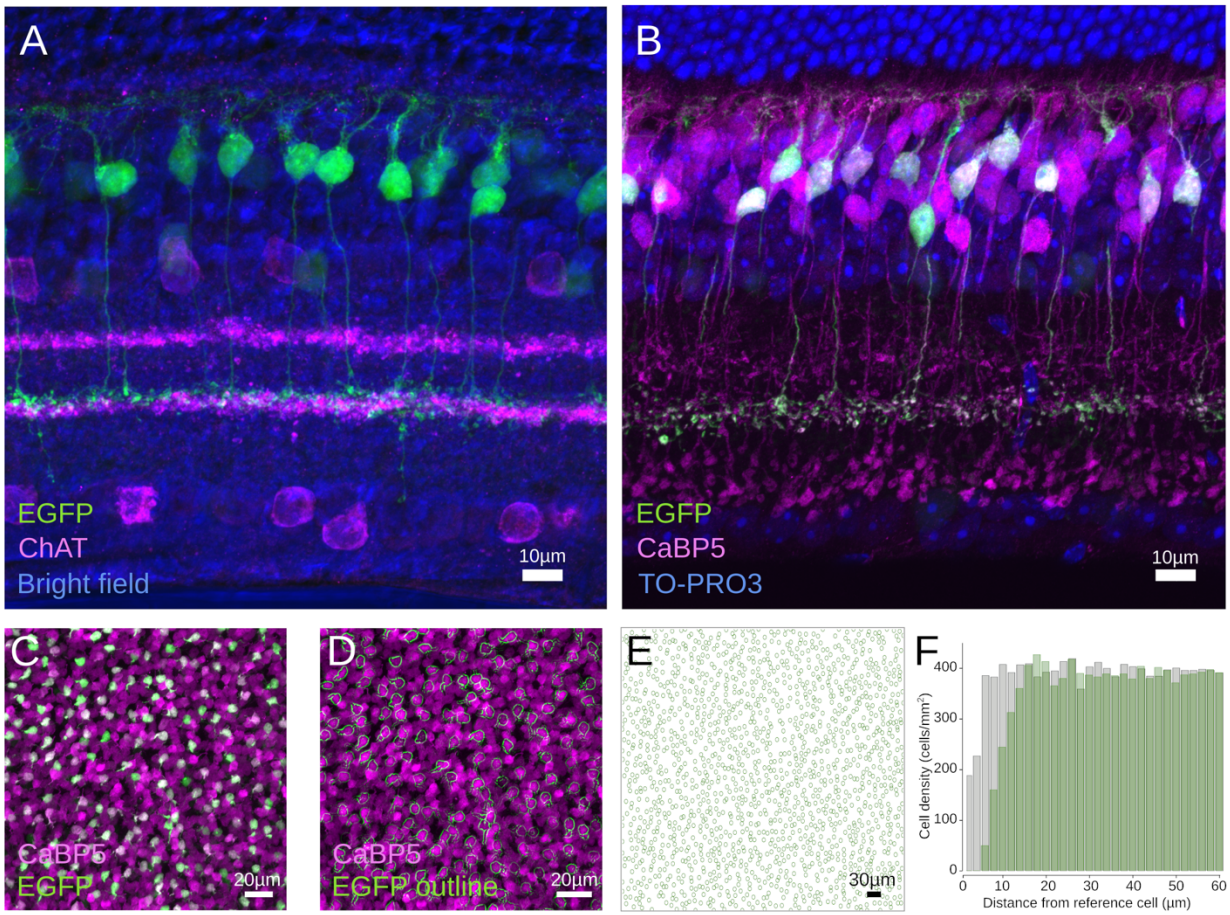

Figure S4. *Characterization of Gjd2-EGFP+ bipolar cells. (A) Vertical section of the Gjd2-EGFP mouse line showing EGFP positive bipolar cells axons (green) stratifying in the ON sublamina of the IPL, co-labeled with cholinergic amacrine cell (magenta, ChAT antibody). Transmitted light image of the retina in blue. (B) Vertical section of the Gjd2-EGFP mouse line showing EGFP positive bipolar cells (green) colocalized with the T5 marker CaBP5 (magenta). (C) En-face image of a whole mount retina from the GJD2 mouse line showing EGFP positive bipolar cells bodies (green) co-labeled with the T5 bipolar cell marker CaBP5 (magenta). (D) Same field as in (C) with cell bodies of EGFP positive bipolar cells outlined (green) by application of a digital edge outlining filter in ImageJ. (E) Position of cell body centroids for EGFP positive bipolar cells in a larger field of view (20X objective) outlined by green circles. (F) Density recovery profile analysis showing the density profile as a function of distance from the reference neuron for EGFP positive bipolar cells (green histograms) and for an equal amount of neurons randomly positioned in the same space (grey histograms) showing the presence of a characteristic exclusion distance for EGFP positive bipolar cells, hallmark of a retinal mosaic.*

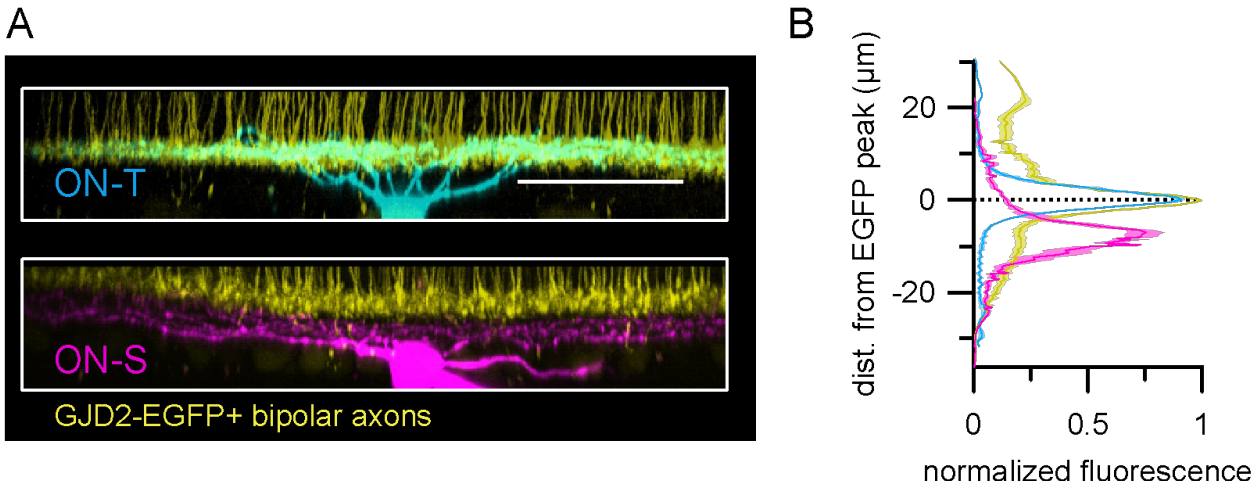

Figure S5. *ON-T and ON-S RGC dendrites ramify in distinct IPL sublaminae. (A) Side projections from 2P z-stack images of dye-filled RGCs (ON-T: top, cyan; ON-S: bottom, magenta) and EGFP signal (yellow) in retinas from Gjd2-EGFP mice. RGCs are same cells as shown in en face view in Fig. 1A (B) Quantification of fluorescence signals from dye filled RGCs in Gjd2-EGFP mouse retina as in (A). Colored lines and shaded areas show mean ± SEM fluorescence intensity with respect to distance from peak EGFP (yellow) fluorescence intensity (n= 6 ON-T, cyan and n= 4 ON-S, magenta, RGCs).*

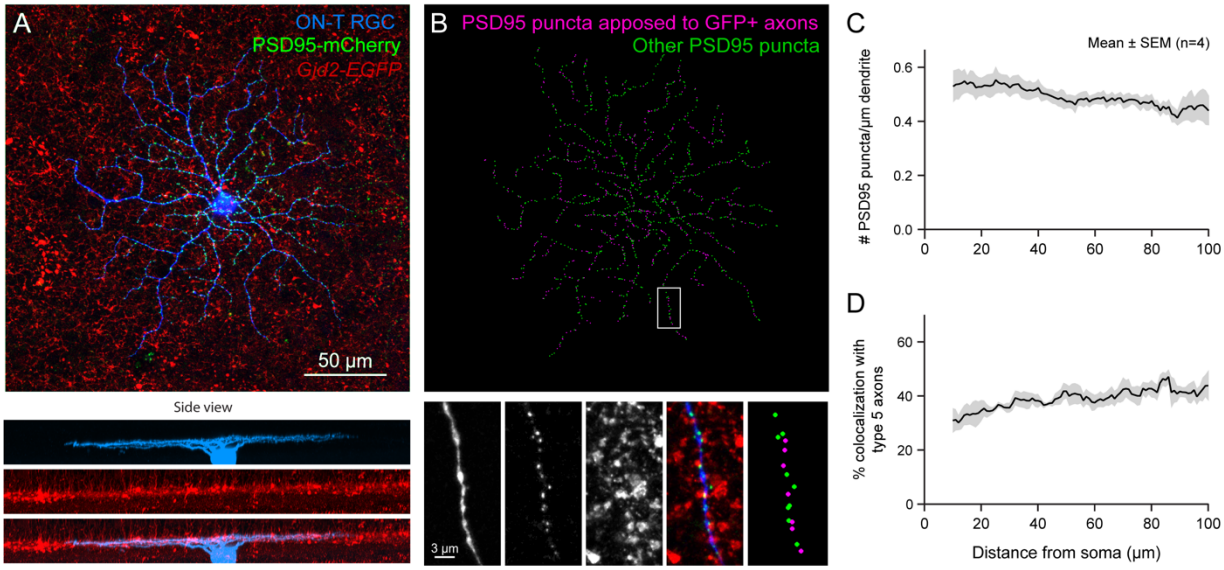

Figure S6. *Gjd2-EGFP+ type 5 bipolar cells provide ~40% of total synapses onto ON-T RGCs. (A) An example ON-T RGC biolistically labeled by Cerulean Fluorescent Protein (blue) and PSD95-mCherry (green) in retina from a Gjd2-EGFP (red) transgenic mouse. Top: en face view, Bottom: side views. (B) Top: Dot map of PSD95-mCherry apposed (magenta) or not apposed (green) to GFP+ BC axon terminals. Bottom: Magnified view of the raw images and the dot map for a segment of dendritic arbor in the while box. (C) Quantification of total excitatory synapse density across the dendritic arbor of ON-T RGCs. (D) Quantification of excitatory synapses in ON-T dendrites that are adjacent to GFP+ axon terminals.*

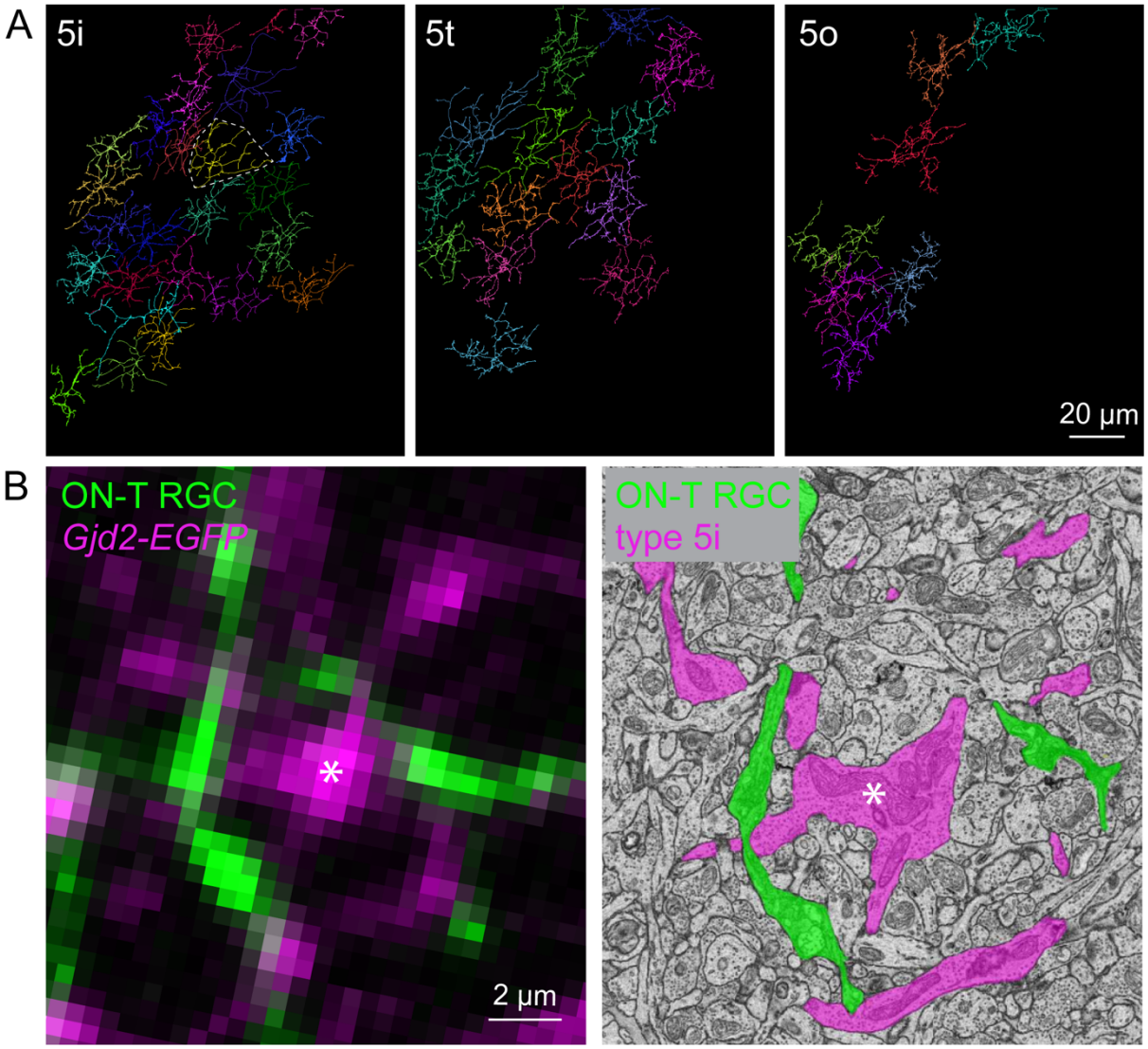

Figure S7. *Classification of three subtypes of type 5 bipolar cells. (A) Wholemount views of the axon terminals of type 5i, type 5t and type 5o bipolar cells in the SBFSEM volume in Fig. 3. The tiling of the space validates the categorization of the three subtypes of type 5 bipolar cells. (B) Identification of Gjd2-EGFP+ bipolar cells as type 5i bipolar cells, supported by correlated light (left) and electron (right) microscopy images. The reconstructed skeleton of the type 5i bipolar cell in (B) is delineated by dashed lines in (A).*

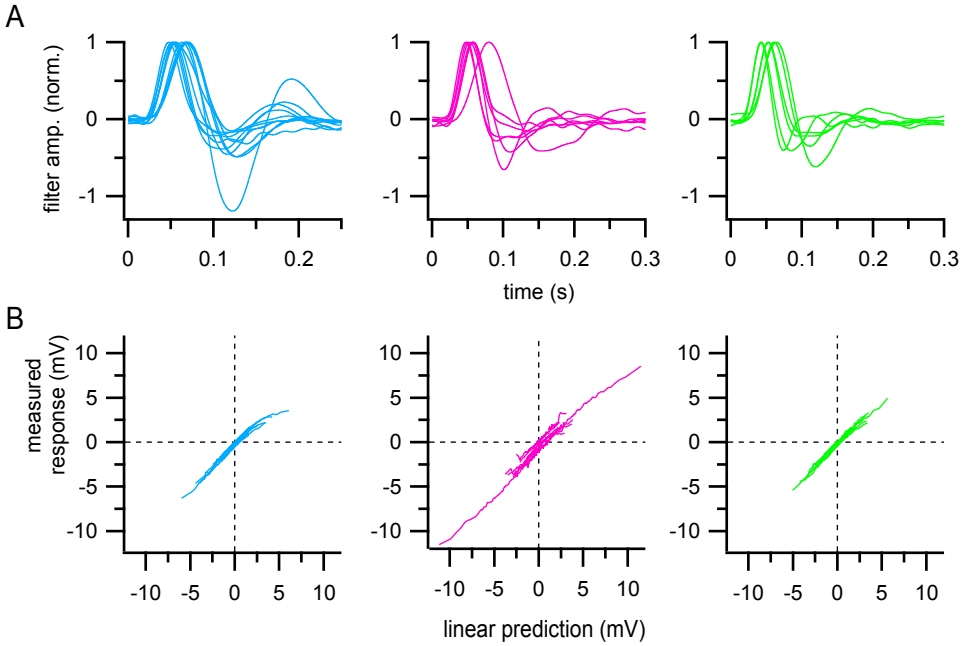

Figure S8. *Linear-nonlinear models of bipolar cell voltage responses. (A) Individual linear filters for all type 5i (cyan; n= 11), type 6 (magenta; n= 7), and type 7 (green; n=6) bipolar cells computed from responses to non-repeated noise stimulus presentation. Filters were normalized to the peak amplitude of the primary inward component to facilitate visual comparison of temporal responses. Same cells as shown in average filters in Fig. 4B. (B) Nonlinearities derived by plotting the predicted response (convolution of linear filter and stimulus) against the measured voltage response for each bipolar cell shown in (A). Linear predictions were calculated using non-normalized filters.*

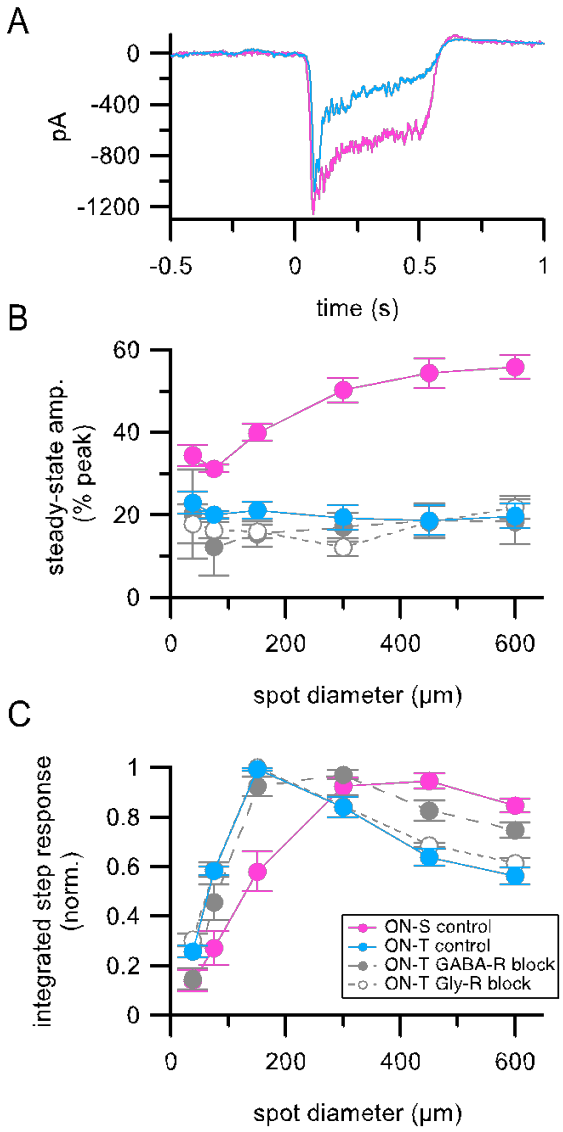

***Figure S9**. Presynaptic inhibition does not affect response kinetics but does affect spatial integration for excitatory inputs to ON-T RGCs (A) Step-evoked (100% contrast, 52 0 µm spot diameter, 500 ms duration) excitatory synaptic currents in example ON-T (cyan) and ON-S RGCs measured in ACSF. Traces show mean responses to ten trials and are baseline subtracted to facilitate comparison. (B) Summary of light step-evoked steady-state response amplitude for different stimulus sizes measured in ACSF. Note that excitatory inputs in ON-T are more transient than those in ON-S RGCs across all stimulus sizes, but responses in both RGC types are more sustained than when measurements were performed using Ames' solution (compare to Fig. 2D-E). (C) Summary of total response, measured as the integrated excitatory current response during the light step, versus stimulus spot size. Responses were normalized to the maximal response in each cell prior to averaging. Excitation in ON-T RGCs is tuned to smaller spot sizes than in ON-S RGCs and this tuning relies in part on GABAergic inhibition. Symbols with error bars in (B) and (C) show mean ± SEM (ON-T control n = 12; ON-S control n = 6; ON-T GABA-R block n = 5; ON-T Gly-R block n = 5).*

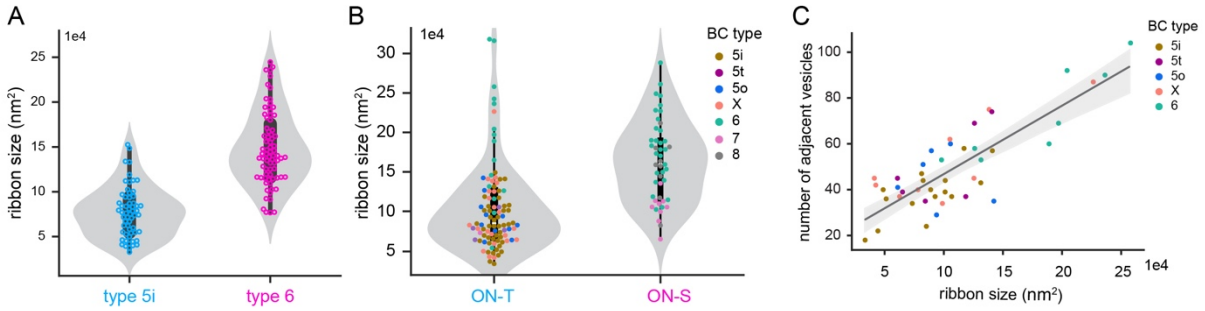

Figure S10. *Bipolar cell subtype-specific differences in ribbon surface areas. (A) Violin plot showing distribution of ribbon surface areas (each data point is a ribbon) for the type 5i and type 6 BC in (Fig 9A). (B) Violin plot with scattered dots showing ribbon surface areas for each ribbon presynaptic to a stretch of reconstructed ON-T or ON-S RGC dendrite. (C) Scatter plot showing ribbon size in surface area in relationship with the number of adjacent vesicles. Gray line represents the linear regression model fitted to the data. Linear regression:* $\beta = 0.0003$, $p < 0.001$, $r^2 = 0.69$.